Systematic characterization of cosmic symplectites in the Acfer 094 carbonaceous chondrite

（炭素質コンドライト Acfer 094 隕石における

宇宙シンプレクタイトの系統的な特徴付け）

By
Kenichi Abe

Department of Natural History Sciences
Graduate School of Science
Hokkaido University

Doctor Thesis
March 2017

ABSTRACT

We describe the petrographic occurrences, abundances, and compositional variations of symplectically intergrown Fe,Ni-sulfides and ^{17,18}O-rich magnetite ($\Delta^{17}O \sim 90‰$), named cosmic symplectites (COS; Sakamoto et al., 2007), from the Acfer 094 (C3.0) ungrouped carbonaceous chondrite. A total of 314 COS studied in two polished sections of this meteorite are uniformly distributed in its matrix with ~600 ppm surface area abundance. No COS have been identified in the Acfer 094 dark inclusions (chondritic lithic clasts) which appear to have experienced extensive aqueous alteration prior to incorporation into the host meteorite. The structure of COS can be arranged in a hierarchy of four categories (from finer to coarser): (1) symplectite structure composed of nanocrystalline magnetite and Fe,Ni-sulfides, (2) submicron-sized wormy structure composed of nanocrystalline symplectites, (3) micrometer-sized irregular rope-like structure composed of wormy structure, and (4) aggregates of the rope-like structure. COS typically associate with fractured Fe,Ni-sulfides and lack Fe,Ni-metal. Most COS studied have smooth surfaces; four grains contain abundant pores. In a single COS, the pore-rich regions are depleted in sulfur and nickel relative to the pore-free regions, indicating that the former are depleted in Fe,Ni-sulfides. Most COS studied contain similar abundances of Fe,Ni-sulfides and magnetite, whereas Ni/(Fe+Ni) atomic ratio in Fe,Ni-sulfides ranges from 0 to 0.4. The lack of Fe,Ni-metal associated with COS supports the formation process proposed by Seto et al. (2008), i.e. oxidation of Fe,Ni-metal and sulfides by ^{17,18}O-rich water vapor in the outer part of the

protoplanetary disk. The similar abundance ratio for Fe,Ni-sulfide and magnetite cannot be simply explained by oxidation processes of Fe,Ni-sulfide precursors after sulfurization of Fe,Ni-metal precursors for COS formation as proposed by Seto et al. (2008).

TABLE OF CONTENTS

LIST OF TABLES

LIST OF FIGURES

INTRODUCTION

Most chondrites consist of three major components – refractory inclusions, chondrules, and fine-grained matrices. On a three-isotope oxygen diagram ($\delta^{17}O$ *vs.* $\delta^{18}O$), compositions of the chondritic components in minimally altered meteorites (petrologic type 3) plot along mass-independent fractionation line with a slope of ~1. This line resulted from mixing of two isotopically distinct nebular reservoirs, ^{16}O-rich and ^{16}O-poor relative to the Standard Mean Ocean Water (SMOW) (Clayton et al., 1973; Yurimoto et al., 2008). The composition of the ^{16}O-rich reservoir is constrained by composition of the Sun ($\Delta^{17}O = -28\pm2‰$) inferred from the solar wind returned by the NASA Genesis mission (McKeegan et al., 2011) and by the compositions of several anomalously ^{16}O-rich ($\Delta^{17}O \sim -35‰$ to $-40‰$) CAIs and a chondrule from CH metal-rich carbonaceous chondrites (Kobayashi et al., 2003; Fujimoto et al., 2009; Gounelle et al., 2009). The nature and composition of the ^{16}O-poor reservoir are poorly known. Aléon et al. (2005) described abundant anomalously $^{17,18}O$-rich ($^{17}O/^{16}O$ and $^{18}O/^{16}O$ ratios are ~0.1) silica-rich grains embedded in the organic residues from the carbonaceous chondrites Orgueil (CI) and Murchison (CM), and attributed these compositions to irradiation of the solar gas by high energy particles accelerated during an active phase of the young Sun. Other researchers suggested that the ^{16}O-poor reservoir was dominated by $^{17,18}O$-rich water ice formed by CO self-shielding either in the protosolar molecular cloud (Yurimoto and Kuramoto, 2004) or in the outer part of the protoplanetary disk (Lyons and Young, 2005). Sakamoto et al. (2007) described

^{17,18}O-rich magnetite-sulfide grains (Δ^{17}O ~ 90‰) in matrix of the ungrouped carbonaceous chondrite Acfer 094 and named them cosmic symplectites (COS). These authors suggested that COS formed by oxidation of Fe,Ni-metal – sulfide particles by ^{17,18}O-rich water vapor in the outer part of the protoplanetary disk.

Cosmic symplectites have a unique chemical composition with Fe:O:S atomic ratio of ~4:4:1 (Sakamoto et al., 2007). A systematic search for COS, based on their chemical compositions, showed that they are ubiquitous in the Acfer 094 matrix (Abe et al., 2008). Mineralogical study of COS (Seto et al., 2008) revealed that they consist of the symplectically intergrown magnetite and pentlandite (Fe5.7Ni3.3S8). Magnetite forms column-shaped grains 10–30 nm in diameter and 100–200 nm in length, whereas pentlandite occurs as worm-shaped grains or aggregates of 100–300-nm-sized grains between magnetite crystals.

Recently, two independent studies confirmed the presence of COS in Acfer 094 (Vollmer et al., 2011; Nittler et al., 2015). In addition, several researchers reported COS-like materials in a primitive CO chondrite Miller Range 07687 (Nittler et al., 2015), chondritic porous interplanetary dust particles possibly of cometary origin (Keller and Messenger, 2011; Starkey et al., 2014), and samples of comet Wild2 returned by the NASA Stardust mission (Nguyen et al., 2014, 2015; Ogliore et al., 2015). However, the mineralogical and petrographic characterizations of COS are still limited. In this study, we performed systematic characterization of COS in Acfer 094 to clarify their abundances, occurrences, chemical compositions, and origin.

SAMPLES AND EXPERIMENTAL PROCEDURES

1.1. SAMPLES

Acfer 094 is an ungrouped carbonaceous chondrite of petrologic type 3.0 with mineralogical, petrological, nitrogen and oxygen isotopic affinities to the CM and CO groups (Newton et al., 1995; Greshake, 1997). Bulk chemical composition of Acfer 094 is similar to those of CM chondrites, whereas bulk oxygen-isotope composition is similar to those of CO chondrites. In contrast to CMs, Acfer 094 experienced incipient aqueous alteration (Wasson and Rubin, 2010; Keller and Messenger, 2012; Hoppe et al., 2015) as indicated by high abundance of presolar silicates, SiC, and diamonds (Newton et al., 1995), and high abundance of amorphous material in its matrix (Greshake, 1997). The meteorite has been subjected to mild terrestrial weathering: its weathering category is W2 (Bischoff and Geiger, 1994).

We studied two polished thin sections of Acfer 094, #1 and #2, coated with a carbon evaporation film of about 30 nm thickness. The section #1, 22×16 mm^2 in size, was previously studied by Sakamoto et al. (2007, 2008), Seto et al. (2008), and Abe et al. (2011). The section #2, 8×5 mm^2 in size, was previously studied by Abe et al. (2008, 2011).

1.2. PROCEDURES OF COS SURVEY

A field-emission scanning electron microscope (FE-SEM, JEOL JSM-7000F) equipped with an energy dispersive X-ray spectrometer (EDS, Oxford INCA Energy) at

Hokkaido University was used for COS survey, which was performed by electron microscopic observations and X-ray elemental mapping. COS grains can be identified in backscattered electron images (BSE): they show intermediate brightness between Fe,Ni-sulfide and magnetite. In order to identify COS more easily and systematically, X-ray elemental maps of a suite of fifteen elements (C, O, Na, Mg, Al, Si, P, S, K, Ca, Ti, Cr, Mn, Fe and Ni) were prepared for fifteen 1×1 mm^2 areas of Acfer 094 (9 and 6 areas in section #1 and #2, respectively). The X-ray elemental maps and BSE images were acquired simultaneously using 15 kV accelerating voltage and 10 nA probe current. Although the X-ray elemental maps have a resolution of 0.2 μm/pixel, their spatial resolution is about 1 μm due to the electron beam broadening in the thin sections. Combined X-ray elemental maps in Fe (red), S (green), and O (blue) were used for the COS survey. COS candidates appear orange in the Fe-S-O combined X-ray map (Abe et al., 2008).

Because both high spatial resolution and broad area are needed for a systematic COS survey, we created several 1×1 mm^2 mosaic maps, each composed of more than four hundred 45×60 μm^2-sized X-ray elemental maps. The smaller maps were set to overlap within ten pixels on each edge. To generate a coordinate file, the BSE images were merged using “Photomerge”, a function of Adobe Photoshop CS series. X-ray elemental maps were subsequently merged by the same coordinate parameter as BSE images using a “MosaicJ”, a function of an ImageJ software.

1.3. PETROGRAPHIC TECHNIQUES

Quantitative analyses for COS grains were performed by FE-SEM-EDS system using 15 kV accelerating voltage, 0.9 nA beam current, and 100 seconds counting time. Analyses with totals outside the range 95−105 wt% and with elemental contributions >2 wt% from the surrounding minerals (i.e. elements except for O, S, Fe and Ni) were discarded.

Because COS consist of nanocrystalline aggregates of Fe-bearing phases – magnetite and Fe,Ni-sulfides (Seto et al., 2008), an (Fe+Ni)/S ratio of sulfides cannot be determined by the low-spatial resolution EDS analysis. In this study, we assumed (Fe,Ni)S stoichiometry of sulfides in COS. All of S and Ni were assigned to (Fe,Ni)S; the remaining iron was assigned to magnetite, which in COS is Ni-free (Seto et al., 2008). Because Fe,Ni-sulfides in COS consist of pentlandite ($(Fe,Ni)_9S_8$) and pyrrhotite ($Fe_{1-x}S$) (Seto et al., 2008, 2010), this assumption can potentially introduce a systematic error of about 10% for the estimated abundances of Fe,Ni-sulfide and magnetite. The error, however, is not sensitive for the discussion in this study.

The number and sizes of COS, Fe,Ni-metal, and sulfide grains, and matrix abundance were measured using 1×1 mm^2 X-ray elemental maps. The grains were selected from the Fe-S-O combined X-ray elemental maps by color threshold setting by each phase using ImageJ. Because many grains have irregular shape, we assumed that their surface areas correspond to volume abundances. The number and size of selected grains were calculated using “Analyze Particles”, a function of the ImageJ. Grains with nine or fewer pixels were discarded as artifacts of the method. Matrix was defined as grains <50 μm in diameter, which is the same definition as that of previous study

(Newton et al., 1995). Grains larger than 50 μm were masked and removed for subsequent image analysis using Photoshop.

RESULTS AND DISCUSSION

1.1. ABUNDANCE OF COS

Figure 1 is a BSE image of the section #2. White squares outline 1×1 mm^2 X-ray elemental mapped regions. Positions of COS identified using Fe-S-O combined X-ray elemental maps and BSE images are indicated by yellow and red circles, respectively. Figure 2a shows one of the 1×1 mm^2-sized Fe-S-O combined X-ray elemental maps, #2-2 (top left outlined region in Fig. 1). The enlarged BSE image and Fe-S-O map (field of view is 80×80 μm^2) of one of the square regions outlined in Figure 2a are shown in Figures 2b and 2c, respectively.

In Fe-S-O maps, chondrules, CAIs and amoeboid olivine aggregates (AOAs) have dark-blue color. Fe,Ni-metal grains, which occur in chondrules, AOAs and as isolated matrix grains, appear red. They are mainly elliptically-shaped and have several tens micrometers in diameter. Fe,Ni-sulfide grains have similar sizes to those of Fe,Ni-metal grains, and appear yellow-green. Iron hydroxides, products of terrestrial weathering, have purple color and occur in veins with/without cracks, and around Fe,Ni-metal grains (Fig. 2a). Magnetite in Acfer 094 is rare; it occurs only in the matrix and shows more reddish and purple color than iron hydroxide. No magnetite except COS magnetite is observed in Figures 2b and 2c under the spatial resolution used.

Matrix filling interstices between large chondritic components appears blue-green. Greshake (1997) reported that the fine-grained matrix of Acfer 094 consists of amorphous material enclosing tiny grains of forsteritic olivine (200–300 nm), enstatitic pyroxene (300–400 nm), and Fe,Ni-sulfides (200–300 nm). Therefore, the blue-green color of fine-grained matrix regions resulted from a mixture of silicates and Fe,Ni-sulfides.

Arrows in Figure 2a show positions of COS identified in the map. Orange region with the size of about 20 μm in the left side of Figure 2c corresponds to a COS. The grain consists of smaller irregular grains of few micrometers in width (Fig. 2b). Tochilinite in CM chondrites, like COS, also consists mainly of Fe, S and O (e.g., Fuchs et al., 1973; Tomeoka and Buseck, 1985). However, because tochilinite contains higher sulfur content than COS, it has dark-green color. Tochilinite-serpentine intergrowths in CM chondrites have color varying from dark-green to purple, depending on the proportion of tochilinite. Therefore, using Fe-S-O maps, COS can be distinguished from other meteorite components.

A total of 314 COS grains from two sections of Acfer 094 have been identified using X-ray elemental maps and BSE images: 160 and 154 grains in sections #1 and #2, respectively. In fifteen 1×1 mm^2 X-ray elemental maps acquired, we identified 157 COS grains. Therefore, the abundance of COS in Acfer 094 is ~10 grains/mm^2; their size distribution is shown in Figure 3. The sizes of COS grains range from 0.6 μm^2 to 931.5 μm^2. The minimum size of COS is consistent with spatial resolution of X-ray elemental maps used in this study. Smaller COS grains are more

abundant and the size distribution appears to follow a power law.

The matrix area in X-ray elemental mapped regions (~15 mm^2) was calculated to be 9.2 mm^2, corresponding to 61.0% of a total area. The similar matrix fraction, ~62.5%, was previously estimated by Newton et al. (1995). An average matrix normalized volume abundance of COS is 611±49 ppm. Nittler et al. (2015) reported the volume abundance of COS as ~230 ppm from the area of 5×10^5 μm^2 which is almost equivalent to the 1×1 mm^2 area in this study. The abundance of COS for 1×1 mm^2 areas ranges from 55 ppm to 2514 ppm. Therefore, the result by Nittler et al. (2015) is in the range of abundance variation within sub millimeter area.

1.2. STRUCTURE OF COS GRAINS

The structure of COS grains can be arranged in a hierarchy of four categories: (1) Symplectite structure composed of nanocrystalline magnetite and Fe,Ni-sulfides (Fig. 5 in Seto et al., 2008). The magnetite crystals have a columnar shape with 10–30 nm diameter and 100–200 nm length; the Fe,Ni-sulfides, 100–300 nm in size, fill the interstices between magnetite crystals. (2) Wormy structure, 100−200 nm in width, composed of symplectites (Fig. 4a). The wormy structure are clearly visible on an ion beam sputtered surface of COS grains. It looks similar to cloudy zone microstructure in iron meteorites formed by a spinodal phase transformation around 300°C during cooling of meteorite parent bodies (e.g., Goldstein et al., 2009). (3) Irregular rope-like structure, few micrometers in width, composed of wormy structure (Fig. 4b). (4) Aggregate of the rope-like structure (Fig. 4c). Texturally, a rope-like structure in the upper part of Figure

4c is similar to COS grain in Figure 4b.

1.3. OCCURRENCES OF COS GRAINS

Figure 5 shows typical occurrences of isolated COS grains or their aggregates embedded in the silicate matrix. COS are often accompanied by Fe,Ni-sulfide grains with a characteristic fractured texture and sometimes are surrounded by them (Fig. 5e). COS attached to Fe,Ni-metal or magnetite have not been observed. About half of COS grains identified are attached to or occurred within iron hydroxide veins formed by terrestrial weathering (Fig. 5g). The textures and chemical compositions of COS in the veins appear to be identical to those in the matrix, suggesting that COS are not easily destroyed by terrestrial weathering. Therefore, the estimated abundance of COS in Acfer 094 of ~600 ppm is probably close to their primary abundance.

In two Acfer 094 thin sections studied, we found eighteen chondritic lithic clasts (dark inclusions (DIs)), ranging from few tens micrometers to 500 μm in diameter (Fig. 6). The mineralogy and petrography of the DIs differ from those of the Acfer 094 matrix: they consist mainly of phyllosilicates, Fe,Ni-sulfide, and magnetite with various morphologies – framboidal, radial, and plaquettes (Figs. 6c,d), suggesting they experienced extensive aqueous alteration prior to incorporation into the host meteorite. In contrast to the virtually anhydrous Acfer 094 matrix containing ~600 ppm of COS, no COS have been identified in the Acfer 094 DIs with a total area of ~0.3 mm^2. The apparent lack of COS in DIs suggests that either COS were initially absent or were efficiently destroyed by aqueous alteration on the DIs parent body(ies).

1.4. CHEMICAL COMPOSITIONS OF COS

Representative chemical compositions of COS are listed in Table 2. Assuming (Fe,Ni)S stoichiometry of sulfides in COS, the estimated ratios of Fe,Ni-sulfide to magnetite range from 0.95 to 1.07 with an average value of 1.02, which is consistent with the previous studies (Sakamoto et al., 2007; Seto et al., 2008). Nickel content of Fe,Ni-sulfide in COS is variable (0−7.3 wt%), corresponding to $0 < Ni/(Fe+Ni)$ atomic ratio < 0.41 with an average value of 0.17.

Although most COS have smooth surfaces, four grains contain abundant tiny pores, <200 nm in diameter (Fig. 7). Fe-S-O maps show that the pore-free regions of the COS have homogeneous orange color similar to those shown in Figure 5. On the other hand, the pore-rich regions appear red-purple in the Fe-S-O map (Fig. 7d), suggesting depletion in sulfur relative to the pore-free regions. In addition, the S-poor regions are also depleted in nickel (Fig. 7c). Because magnetite in COS does not contain nickel, the S-poor regions must be depleted in Fe,Ni-sulfides. The texture and chemical composition suggest that the pore-rich COS may be a transit stage towards decomposition of COS by aqueous alteration. If so, nano-magnetite particles genetically related to COS may have survived in matrices of weakly aqueously altered carbonaceous chondrites and could be identified as ^{17,18}O-rich phase in the future.

1.5. SIZE DISTRIBUTIONS OF COS

Size distributions of COS, Fe,Ni-metal, and Fe,Ni-sulfides in the Acfer 094

matrix were obtained from fifteen 1×1 mm^2 X-ray elemental maps. We identified 157 grains of COS, 1294 grains of Fe,Ni-metal, and 32181 grains of Fe,Ni-sulfide. Based on the textural appearance, Fe,Ni-sulfides in Acfer 094 can be classified into two categories: fractured and unfractured. Out of 32181 Fe,Ni-sulfide grains, only 374 (~1%) belong to the category of fractured grains.

Figure 8 shows a relative cumulative size distribution of COS, Fe,Ni-metal, unfractured (normal) Fe,Ni-sulfide, and fractured Fe,Ni-sulfide in the Acfer 094 matrix. The cumulative frequency of unfractured Fe,Ni-sulfides defines a straight line throughout all size range from 1 to 1000 μm^2, indicating that the number of smaller grains increases according to a power law. The distribution of Fe,Ni-metal grains follows an arch. The distribution of COS grains in the range of 10 to 200 μm^2 follows a straight line with a slope steeper than that of Fe,Ni-metal and more gentle than that of unfractured Fe,Ni-sulfide. The distribution of fractured Fe,Ni-sulfide grains is different from that of unfractured Fe,Ni-sulfide, and for the grains in the range of 10−200 μm^2 appears to follow a straight line with a slope similar to that of COS. Because COS are thought to have formed by oxidation of Fe,Ni-sulfides±Fe,Ni-metal (Sakamoto et al., 2007; Seto et al., 2008), the similar occurrences and grain size distributions of the fractured Fe,Ni-sulfides and COS imply their genetic relationship.

1.6. IMPLICATION FOR THE ORIGIN OF COS

Seto et al. (2008) proposed a formation process of COS based on their crystal-chemical properties. These authors suggested that one of the possible COS

precursors was martensitic Fe,Ni-metal condensed from a gas of solar composition at temperature and pH_2S/pH_2 ratio corresponding to a segment AB in Figure 9. Subsequently the Fe,Ni-metal was sulfurized by H_2S gas to form Fe,Ni-sulfides with wormy textures by cooling from 700 K to 360 K (B → C in Fig. 9) with a cooling rate of ~100 K/day. Because nickel solubility in mss decreases with a temperature decrease (Mirsa and Fleet, 1973; Naldrett, 2004), the excessive nickel was exsolved as pentlandite, and a lamellar texture composed of mss and pentlandite was developed. At ~360 K, the mineral assemblage consisted of troilite, pentlandite, and ±Fe,Ni-metal (point C in Fig. 9). Below ~360 K, troilite and Fe,Ni-metal were oxidized by water vapor to form magnetite (Urey, 1952; Fegley, 2000; Sakamoto et al., 2007) (point D in Fig. 9); pentlandite survived the oxidation. As a result, the exsolution texture of troilite-pentlandite assemblage changed to a symplectite texture of magnetite-pentlandite assemblage. This process is consistent with apparent lack of Fe,Ni-metal in COS grains studied.

Another possible precursor of COS considered by Seto et al. (2008) consisted of pentlandite and troilite. Troilite was subsequently oxidized by water vapor to form magnetite; pentlandite and some troilite survived the oxidation. Because Fe,Ni-sulfide/magnetite ratio in COS grains studied is about 1 and the highest Ni/(Fe+Ni) ratio in Fe,Ni-sulfides is 0.41 which is COS #17 of Seto et al. (2008), the estimated pentlandite/troilite ratio in COS precursors is about 1/3 (Fig. 10). The sulfide/magnetite ratio may vary if troilite partly survived the oxidation as indicated by a dashed line in Figure 10. In fact, pyrrhotite-pentlandite-magnetite assemblage was

reported in Ni-poor COS grains (Seto et al., 2010). Ni/(Fe+Ni) ratio of Fe,Ni-sulfides in COS grains studied ranges from 0.41 to 0, whereas Fe,Ni-sulfide/magnetite ratio is nearly constant, ~1 (Fig. 10). Based on these observations, we infer that Fe,Ni-sulfide precursors of COS had variable Ni/(Fe+Ni) ratios and were oxidized to about 75% to form magnetite. The similar oxidation degrees among COS grains suggest that COS formation occurred in a condition with a unique oxygen fugacity. Chemical analysis of individual nano-grains of Fe,Ni-sulfides of COS would be helpful to infer the oxygen fugacity.

CONCLUSIONS

1. We have identified 314 COS grains in two thin sections of Acfer 094. 157 grains of these were identified using X-ray elemental maps acquired with a 1 μm spatial resolution. COS grains are ubiquitously distributed in the Acfer 094 matrix with ~600 ppm surface area abundance.

2. The structure of COS grains can be arranged in a hierarchy of four categories: (1) symplectic structure composed of nanocrystalline magnetite and Fe,Ni-sulfide, (2) submicron-sized wormy structure composed of the symplectite structure, (3) irregular rope-like structure with micrometer width composed of the wormy structure, and (4) aggregates of the rope-like structure.

3. COS grains riddled with dark pores are very rare (only 4 grains studied belong to this category). Pore-rich regions of the COS grains are depleted in Fe,Ni-sulfide components. This texture may have formed by eroding of the COS grains. The effect of terrestrial

weathering on COS might be very limited because the texture and chemical composition of COS grains found in terrestrial weathering veins were similar to those of COS in the matrix. The lack of COSs in the heavily aqueously altered Acfer 094 dark inclusions suggests that either COS were decomposed during aqueous alteration experienced by the dark inclusions on their parent body(ies), or the dark inclusions initially lacked COS. If the former is the case, the presence of pore-rich COS may represent the initial stages of decomposition of COS by aqueous alteration.

4. Most COS studied contain similar abundances of Fe,Ni-sulfides and magnetite, whereas Ni/(Fe+Ni) atomic ratio in Fe,Ni-sulfides ranges from 0 to 0.4. The lack of Fe,Ni-metal associated with COS supports the formation process proposed by Seto et al. (2008), i.e. oxidation of Fe,Ni-metal and sulfides by ^{17,18}O-rich water vapor in the outer part of the protoplanetary disk. The similar abundance ratio for Fe,Ni-sulfides and magnetite cannot be simply explained by oxidation processes of Fe,Ni-sulfide precursors after sulfurization of Fe,Ni-metal precursors for COS formation as proposed by Seto et al. (2008).

ACKNOWLEDGEMENTS

I am indebted to Professor H. Yurimoto. I am grateful to him for numerous valuable suggestions and his kind support throughout this work. I have learned many things in the field of cosmochemistry from him.

I deeply thank to Dr. N. Sakamoto for his helpful suggestion, discussions, and encouragements. I thank to other members of my doctoral committee, Professor T. Nagai and Dr. S. Tachibana for their advices and valuable comments.

I am grateful to other staffs, students, former members of Yurimoto-Lab, and Dr. A. N. Krot for many helpful suggestions and encouragements.

Acfer 094 sections were provided by the Museum für Naturkunde, Berlin.

REFERENCES

Abe, K., Sakamoto, N., Krot, A. N. and Yurimoto, H. (2008) Abundaces of new-PCP in Acfer 094 and other carbonaceous chondrites. *39th Lunar and Planetary Science Conference*, #1509 (Abstract).

Abe, K., Sakamoto, N., Krot, A. N. and Yurimoto, H. (2011) Abundance of cosmic symplectite in Acfer 094 carbonaceous chondrite. *Workshop on Formation of the First Solids in the Solar System*, p.9043 (Abstract).

Aléon, J., Robert, F., Duprat, J., and Derenne, S. (2005) Extreme oxygen isotope ratios in the early Solar System. *Nature* **437**, 385–388.

Bischoff, A. and Geiger, T. (1994) The unique carbonaceous chondrite Acfer 094: The first CM3 chondrite (?). *25th Lunar and Planetary Science Conference*, pp.115–116.

Clayton, R. N., Grossman, L. and Mayeda, T. K. (1973) A Component of primitive nuclear composition in carbonaceous meteorites. *Science* **182**, 485–488.

Fegley, Jr. B. (2000) Kinetics of gas-grain reactions in the solar nebula. *Space Science Review* **92**, 177−200.

Fuchs, L. H., Olsen E. and Jensen K. J. (1973) Mineralogy, mineral-chemistry, and composition of the Murchison (C2) meteorite. *Smithsonian Contributions to the Earth Sciences* **10**, 1–39.

Fujimoto, K., Itoh, S., Ebata, S. and Yurimoto, H. (2009) Non-chondritic oxygen isotopic component of metals in a noble-gas-rich chondrite—vestige of stellar wind from the protosun? *Geochemical Journal* **43**, e11–e15.

Greshake, A. (1997) The primitive matrix components of the unique carbonaceous

chondrite Acfer 094: A TEM study. *Geochimica et Cosmochimica Acta* **61**, 437–452.

Goldstein, J. I., Yang, J., Kotula, P. G. Michael, J. R. and Scott, E. R. D. (2009) Thermal histories of IVA iron meteorites from transmission electron microscopy of the cloudy zone microstructure. *Meteoritics & Planetary Science* **44**, 343–358.

Gounelle, M., Krot, A. N., Nagashima, K. and Kearsley, A. (2009) Extreme 16O enrichment in Calcium-Aluminum-rich inclusions from the Isheyevo (CH/CB) chondrite. *The Astrophysical Journal Letters* **698**, L18–L22.

Hoppe, P., Leitner, J., and Kodolányi, J. (2015) New constraints on the abundances of silicate and oxide stardust from supernovae in the Acfer 094 meteorite. *The Astrophysical Journal Letters* **808**, L9.

Keller, L. P., and Messenger, S. (2011) On the origins of GEMS grains. *Geochimica et Cosmochimica Acta* **75**, 5336–5365.

Keller, L. P., and Messenger, S. (2012) Formation and processing of amorphous silicates in primitive carbonaceous chondrites and cometary dust. *43rd Lunar and Planetary Science Conference*, #1880 (Abstract).

Kobayashi, S., Imai, H. and Yurimoto, H. (2003) New extreme 16O-rich reservoir in the early solar system. *Geochemical Journal* **37**, 663–669.

Lyons, J. R. and Young, E. D. (2005) CO self-shielding as the origin of oxygen isotope anomalies in the early solar nebula. *Nature* **435**, 317–320.

McKeegan, K. D., Kallio, A. P. A., Heber, V. S., Jarzebinski, G., Mao, P. H., Coath, C. D., Kunihiro, T., Wiens, R. C., Nordholt, J. E., Moses, Jr. R. W., Reisenfeld, D. B., Jurewicz, A. J. G. and Burnett, D. S. (2011) The oxygen isotopic composition of the Sun inferred from captured solar wind. *Science* **332**, 1528–

1532.

Mirsa, K. and Fleet, M. E. (1973) The chemical compositions of synthetic and natural pentlandite assemblages. *Economic Geology* **68**, 518–539.

Naldrett, A. J. (2004) Magmatic sulfide deposits; Geology, geochemistry and exploration. *Springer Science & Business Media*.

Newton, J., Bischoff, A., Arden, J. W., Franchi, I. A., Geiger, T., Greshake, A. and Pillinger, C. T. (1995) Acfer 094, a uniquely primitive carbonaceous chondrite from the Sahara. *Meteoritics* **30**, 47–56.

Nguyen, A. N., Berger, E. L., Nakamura-Messenger, K. and Messenger, S. (2014) Coordinated mineralogical and isotopic analysis of a cosmic symplectite identified in a stardust terminal particle. *77th Annual Meteoritical Society Meeting*, #5388 (Abstract).

Nguyen, A. N., Berger, E. L., Nakamura-Messenger, K., and Messenger, S. (2015) Sulfur and oxygen isotopic analysis of a cosmic symplectite from a comet Wild 2 stardust terminal particle. *78th Annual Meeting of the Meteoritical Society*, #5375 (Abstract).

Nittler, L. R., Davidson, J., Liu, N., Alexander, C. M. O'D., and Stroud, R. M. (2015) A search for cosmic symplectite in the Acfer 094 and Miller Range 07687 meteorites. *46th Lunar and Planetary Science Conference*, #2097 (Abstract).

Ogliore, R. C., Nagashima, K., Huss, G. R., Westphal, A. J., Gainsforth, Z., Butterworth, A. L. (2015) Oxygen isotopic composition of coarse- and fine-grained material from comet 81P/Wild 2. *Geochimica et Cosmochimica Acta* **166**, 74–91.

Sakamoto, N., Seto, Y., Itoh, S., Kuramoto, K., Fujino, K., Nagashima, K., Krot, A. N. and Yurimoto, H. (2007) Remnants of the early solar system water enriched in heavy oxygen isotopes. *Science* **317**, 231–233.

Sakamoto, N., Itoh, S. and Yurimoto, H. (2008) Discovery of 17,18O-rich material from meteorite by direct-imaging method using stigmatic-SIMS and 2D ion detector. *Applied Surface Science* **255**, 1458–1460.

Seto, Y., Sakamoto, N., Fujino, K., Kaito, T., Oikawa, T. and Yurimoto, H. (2008) Mineralogical characterization of a unique material having heavy oxygen isotope anomaly in matrix of the primitive carbonaceous chondrite Acfer 094. *Geochimica et Cosmochimica Acta* **72**, 2723–2734.

Seto, Y., Toh, S., Sakamoto, N. and Yurimoto, H. (2010) Microstructure and its origin of isotopically anomalous material COS in the Acfer 094 carbonaceous chondrite. *2010 JAMS Annual Meeting*, abstract p.157 (in Japanese).

Starkey, N. A., Franchi, I. A. and Lee, M. R. (2014) Isotopic diversity in interplanetary dust particles and preservation of extreme 16O-depletion. *Geochimica et Cosmochimica Acta* **142**, 115–131.

Tomeoka, K. and Buseck, P. R. (1985) Indicators of aqueous alteration in CM carbonaceous chondrites: Microtextures of a layered mineral containing Fe, S, O and Ni. *Geochimica et Cosmochimica Acta* **49**, 2149–2163.

Urey, H. C. (1952) The Planets: Their origin and development. *Yale University Press*, p. 245.

Vollmer, C., Leitner, J., Busemann, H., Spring, N. and Hoppe, P. (2011) The association of 15N-anomalous matter with stardust in chondrites Acfer 094 and Northwest Africa 852. *42nd Lunar and Planetary Science Conference*, #1720 (Abstract).

Wasson, J. T. and Rubin, A. E. (2010) Matrix and whole-rock fractionations in the Acfer 094 type 3.0 ungrouped carbonaceous chondrite. *Meteoritics & Planetary Science* **45**, 73–90.

Yurimoto, H. and Kuramoto, K. (2004) Molecular cloud origin for the oxygen isotope heterogeneity in the solar system. *Science* **305**, 1763–1766.

Yurimoto, H., Krot, A. N., Choi, B.-G., Aleon, J., Kunihiro, T. and Brearley, A. J. (2008) Oxygen Isotopes of Chondritic Components. *Rev. Mineralogy and Geochemistry* **68**, 141–186.

Table 1. Abundance of COS in the Acfer 094 matrix estimated from X-ray elemental maps of 1×1 mm^2 area.

Section	Map	Matrix (%)	Frequency (count)	Average size (μm2)	Abundance (ppm)
#1	1	48.9	9	16.6	306
	2	44.2	8	29.2	548
	3	64.3	5	14.4	116
	4	68.0	19	27.6	732
	5	58.5	2	16.6	55
	6	67.9	13	134.0	2514
	7	71.9	10	29.1	425
	8	64.6	18	21.1	578
	9	51.0	4	12.2	95
#2	1	65.5	10	23.3	344
	2	63.2	15	41.7	956
	3	60.4	14	16.2	382
	4	66.2	5	121.6	945
	5	59.2	14	14.6	342
	6	60.8	11	24.5	423
total		61.0	157	35.9	611

Table 2. Chemical composition of COS

	#014	#015	#017	#019	#020	#021	#022	#024	#025	#027	#062	#068	#070
Weight %													
FeO*	21.7	21.3	22.9	22.3	22.2	21.6	22.0	21.6	22.2	22.5	21.8	22.1	22.2
Fe_2O_3*	48.1	47.4	51.0	49.6	49.4	48.0	48.8	48.0	49.3	50.1	48.4	49.1	49.4
Na_2O	*n.d.	n.d.	n.d.	n.d.	n.d.	n.d.	n.d.	n.d.	n.d.	n.d.	n.d.	0.2	n.d.
MgO	n.d.	0.4	n.d.	n.d.	0.2	0.2	n.d.	n.d.	n.d.	0.2	0.2	0.5	n.d.
Al_2O_3	n.d.	n.d.	n.d.	n.d.	0.2	n.d.	n.d.	n.d.	n.d.	n.d.	0.1	n.d.	n.d.
SiO_2	0.3	1.1	n.d.	0.5	n.d.	0.3	n.d.	n.d.	n.d.	n.d.	0.4	0.6	0.4
CaO	0.2	n.d.	0.1	0.2	n.d.	n.d.	n.d.	n.d.	n.d.	n.d.	0.2	n.d.	n.d.
Fe	16.3	16.1	9.9	14.0	12.2	17.1	13.8	13.1	11.9	13.2	16.0	15.5	15.1
Ni	1.0	0.5	7.3	2.7	5.5	0.7	3.6	4.7	5.2	3.5	2.2	2.7	2.8
S	9.9	9.5	9.7	9.5	10.0	10.2	9.9	10.1	9.7	9.5	10.4	10.4	10.2
total	97.5	96.3	100.9	98.8	99.7	98.1	98.1	97.5	98.4	99.0	99.8	101.1	100.2
Oxidized atom # (assumed O ≡ 4)													
Fe	2.93	3.00	3.16	3.15	2.97	2.84	2.97	2.86	3.06	3.17	2.81	2.85	2.92
Sulfurized atom # (assumed S ≡ 1)													
Fe	0.94	0.97	0.59	0.84	0.70	0.96	0.80	0.75	0.71	0.80	0.88	0.86	0.85
Ni	0.06	0.03	0.41	0.16	0.30	0.04	0.20	0.25	0.29	0.20	0.12	0.14	0.15
(Fe,Ni)S/Fe_3O_4	1.02	1.00	0.95	0.95	1.01	1.06	1.01	1.05	0.98	0.95	1.07	1.05	1.03

	#071	#075	#084	#090	#091	#097	#100	#106	#107	#111	#112	#116	#119
Weight %													
FeO*	21.9	22.3	22.3	21.8	21.6	22.1	22.0	21.5	21.6	22.0	22.2	21.1	22.1
Fe_2O_3*	48.6	49.5	49.6	48.5	48.1	49.2	48.8	47.7	47.9	48.9	49.3	46.9	49.1
Na_2O	n.d.	n.d.	n.d.	n.d.	n.d.	n.d.	n.d.	n.d.	n.d.	n.d.	n.d.	n.d.	n.d.
MgO	n.d.	n.d.	n.d.	n.d.	n.d.	0.6	n.d.	0.2	0.3	0.3	n.d.	n.d.	n.d.
Al_2O_3	0.2	n.d.	n.d.	n.d.	n.d.	n.d.	n.d.	n.d.	n.d.	0.2	n.d.	n.d.	n.d.
SiO_2	0.3	0.4	0.4	0.4	0.3	1.1	0.3	0.3	0.7	0.6	0.2	0.7	0.3
CaO	n.d.	n.d.	n.d.	n.d.	n.d.	n.d.	n.d.	n.d.	0.2	n.d.	n.d.	0.1	n.d.
Fe	16.4	11.8	12.5	15.9	17.6	12.3	16.3	15.0	16.2	13.6	12.9	14.6	15.9
Ni	1.8	5.7	5.1	1.6	n.d.	4.4	1.5	2.4	0.9	4.2	4.9	2.9	2.0
S	10.4	9.9	10.0	10.0	10.1	9.5	10.1	9.9	9.8	10.1	10.1	10.0	10.2
total	99.6	99.6	99.9	98.2	97.7	99.3	98.9	97.0	97.5	99.9	99.6	96.3	99.6
Oxidized atom # (assumed O ≡ 4)													
Fe	2.82	3.01	3.00	2.92	2.87	3.12	2.90	2.89	2.95	2.92	2.95	2.83	2.89
Sulfurized atom # (assumed S ≡ 1)													
Fe	0.91	0.69	0.72	0.91	1.00	0.75	0.92	0.87	0.95	0.77	0.73	0.84	0.89
Ni	0.09	0.31	0.28	0.09	0.00	0.25	0.08	0.13	0.05	0.23	0.27	0.16	0.11
(Fe,Ni)S/Fe_3O_4	1.06	1.00	1.00	1.03	1.04	0.96	1.03	1.04	1.02	1.03	1.02	1.06	1.04

*molar ratios of FeO/Fe_2O_3 is assumed as unity because Fe-oxides contained in magnetite phase.

*n.d.: not detected

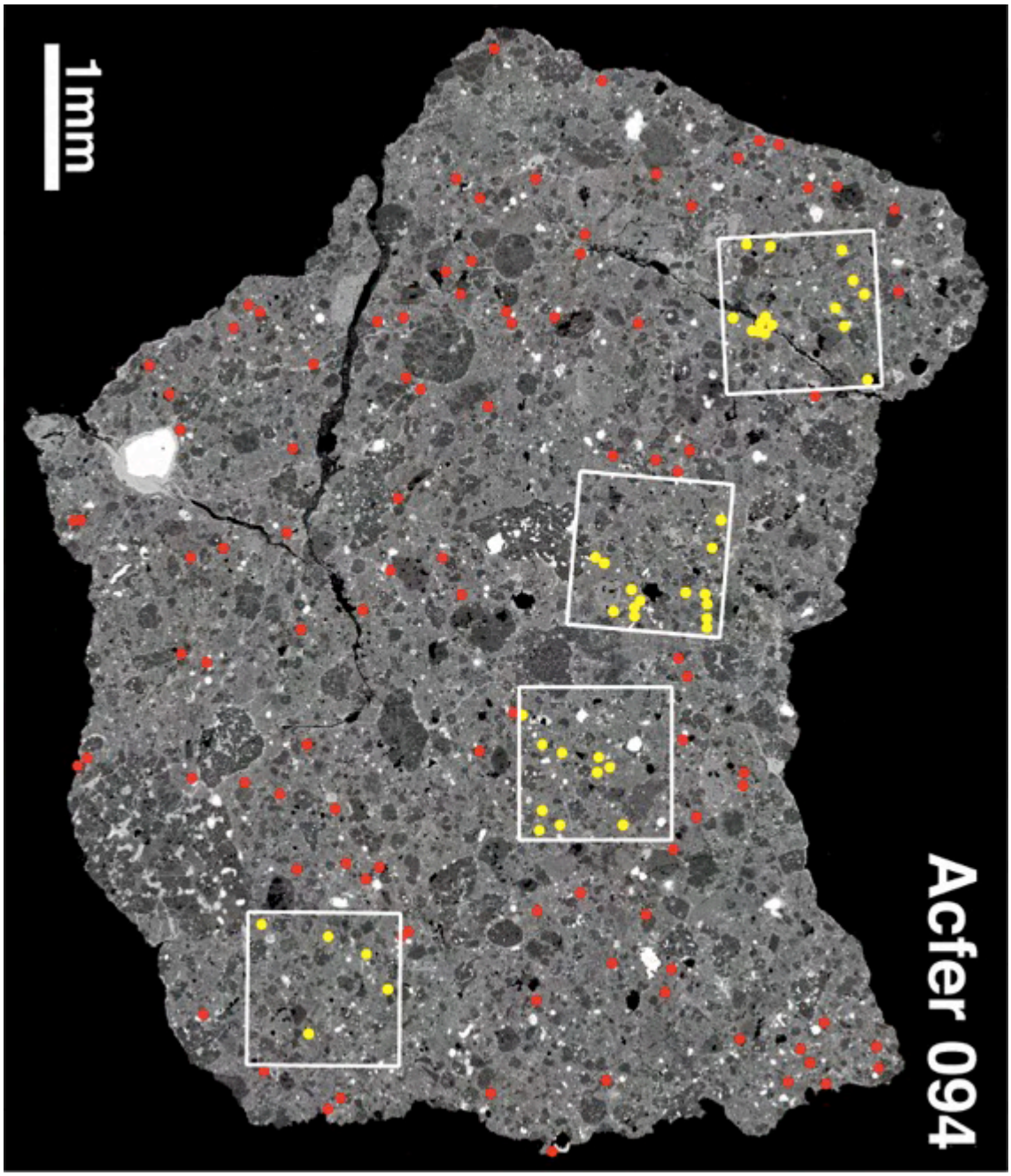

Fig. 1. Backscattered electron image of the entire thin section of Acfer 094#2. Red and yellow circles show COS positions identified by the electron microscope observation and by the X-ray elemental mapping technique, respectively. White squares correspond to the X-ray elemental mapped regions of a 1×1 mm area. The squares are named as Acfer 094#2-2, 2-3, 2-1 and 2-4 from left to right.

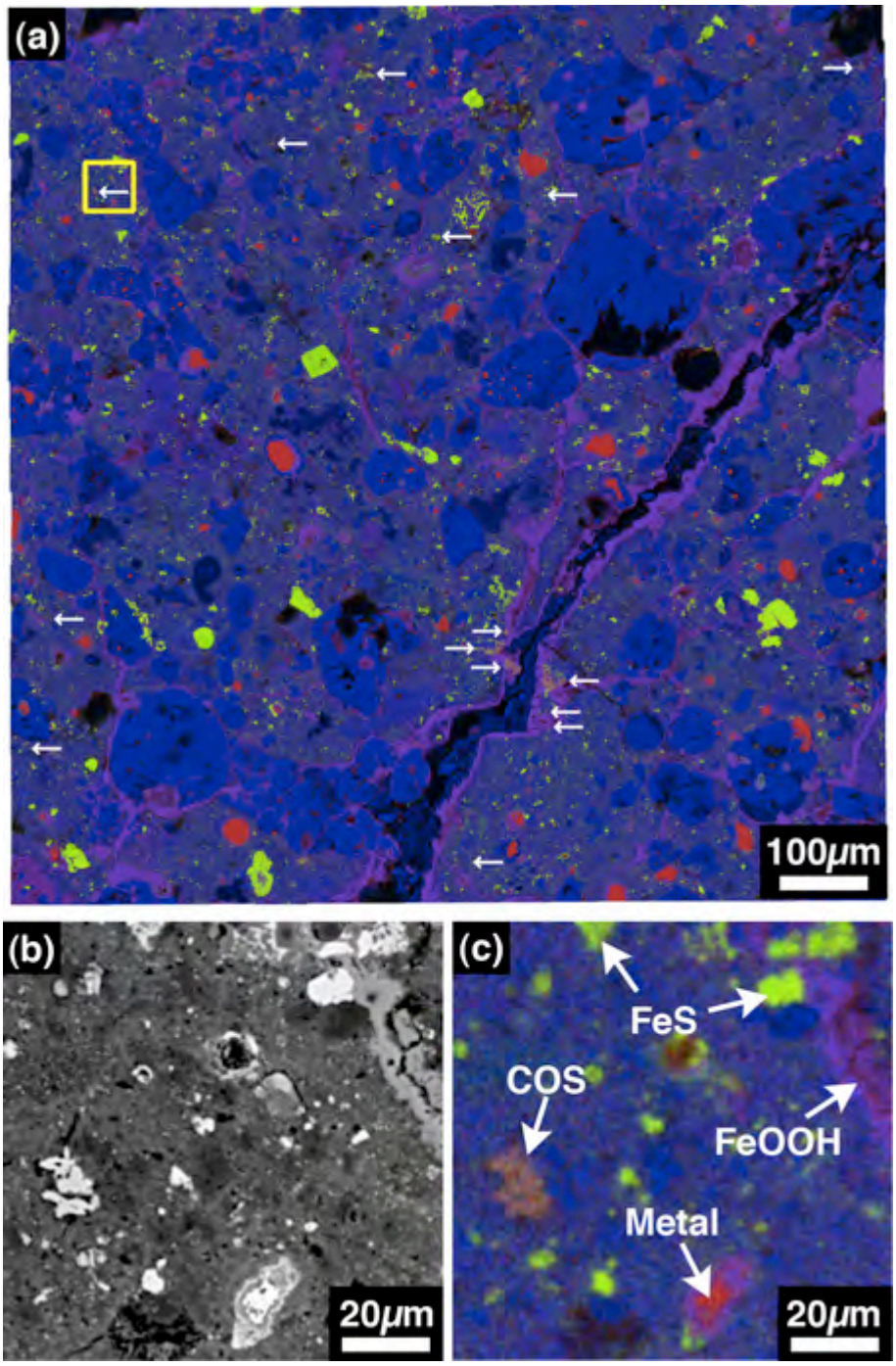

Fig. 2. (a) RGB color composite map assigned red to Fe, green to S and blue to O (Fe-S-O map) for Acfer 094#2-2. Arrows show the positions of COS grains. The grains of Fe,Ni-metal, iron sulfide and COS appear red, yellow-green and orange color in the Fe-S-O map, respectively. Enlarged (b) backscattered electron image and (c) Fe-S-O map of the square region in (a).

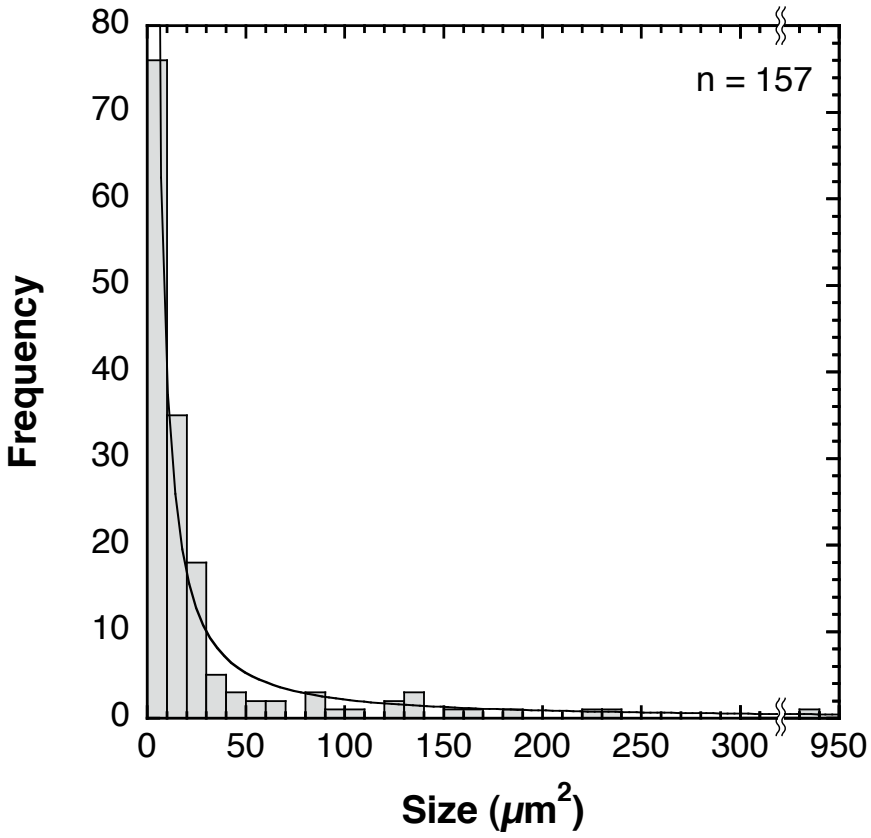

Fig. 3. Size distribution of COS grains. A power law function of $\boldsymbol{y = 746.28 \times x^{-1.268}}$ is shown in figure.

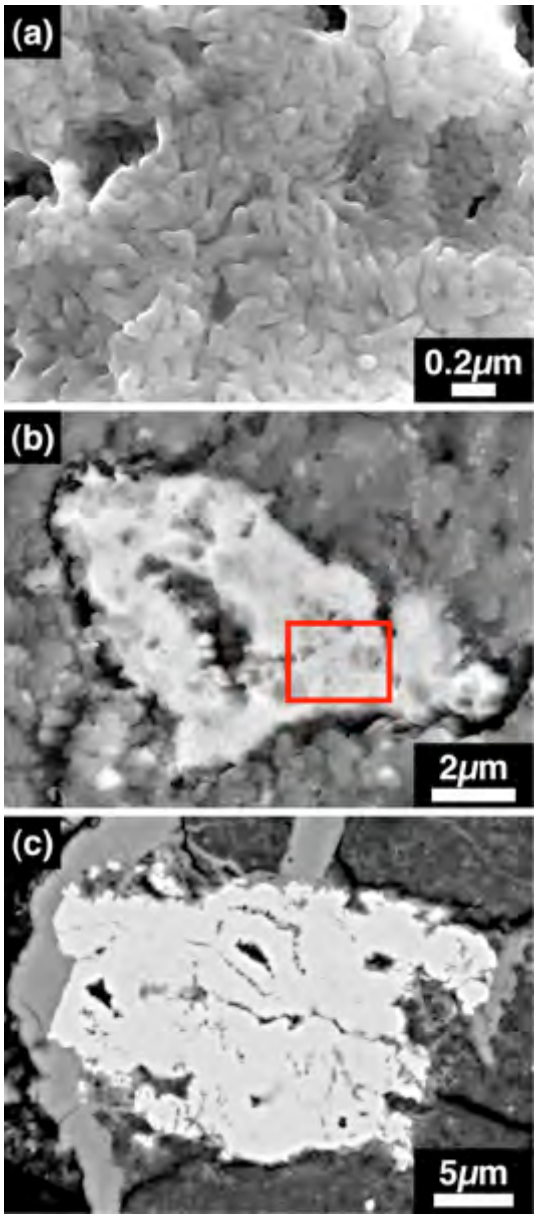

Fig. 4. Morphology of COS. (a) High-magnification secondary electron image of the rectangle region in (b) showing a surface of COS #15 after Cs^+ ion sputtering by SIMS. (b) Backscattered electron (BSE) image after the ion sputtering for entire grain of COS #15 showing a rope-like structure. (c) BSE image for aggregate of rope-like structures on polished surface.

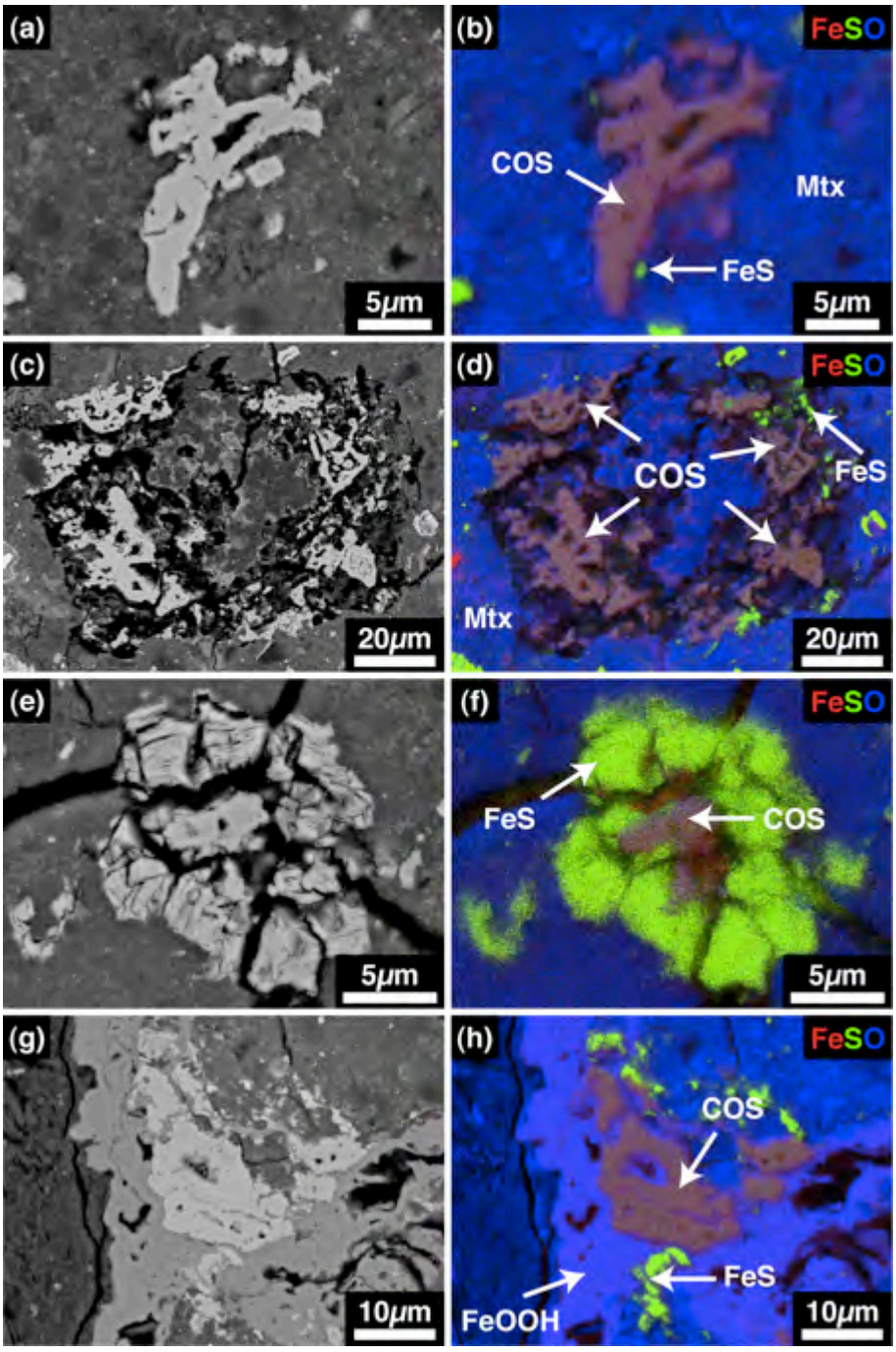

Fig. 5. Typical occurrences of COS in the Acfer 094. (a,c,e,g) Backscattered electron images. (b,d,f,h) RGB color composite map assigned red to Fe, green to S and blue to O (Fe-S-O map). Fe,Ni-metal, Fe,Ni-sulfide and COS appear red, yellow-green and orange color in the Fe-S-O map, respectively. (a,b) COS grain independently embedded in the matrix silicate. (c,d) Aggregate of COS grains. (e,f) COS grain surrounded by fractured Fe,Ni-sulfide grains. (g,h) COS grain attached to terrestrial weathering vein.

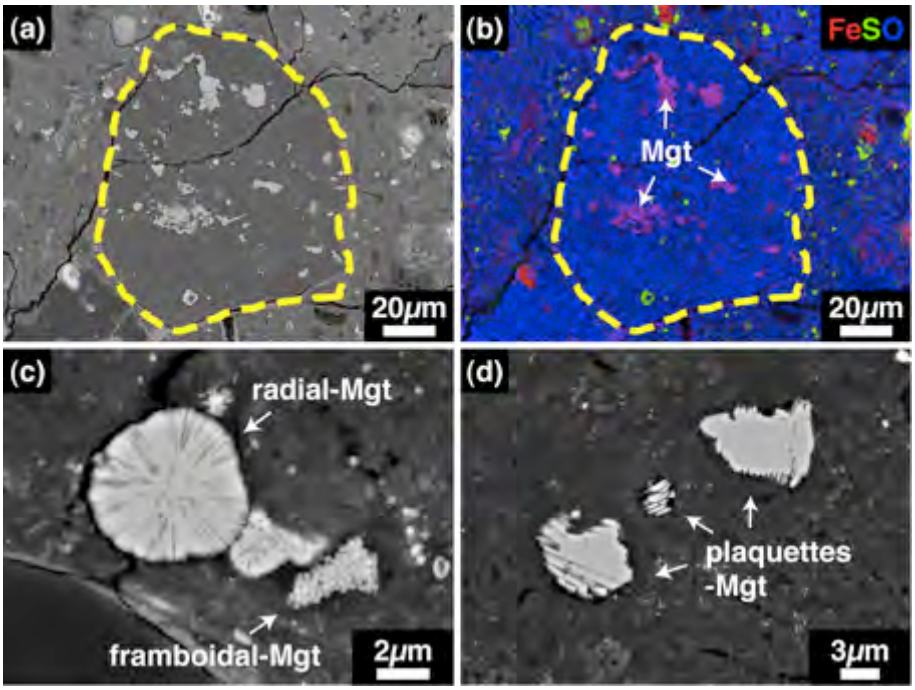

Fig. 6. (a) Backscattered electron (BSE) image and (b) Fe-S-O composite map of a dark inclusion in the Acfer 094. The yellow dashed line marks approximate boundary of the dark inclusion. BSE images of magnetite (Mgt) grains showing (c) framboidal, radial and (d) plaquettes shapes observed in the Acfer 094 dark inclusions.

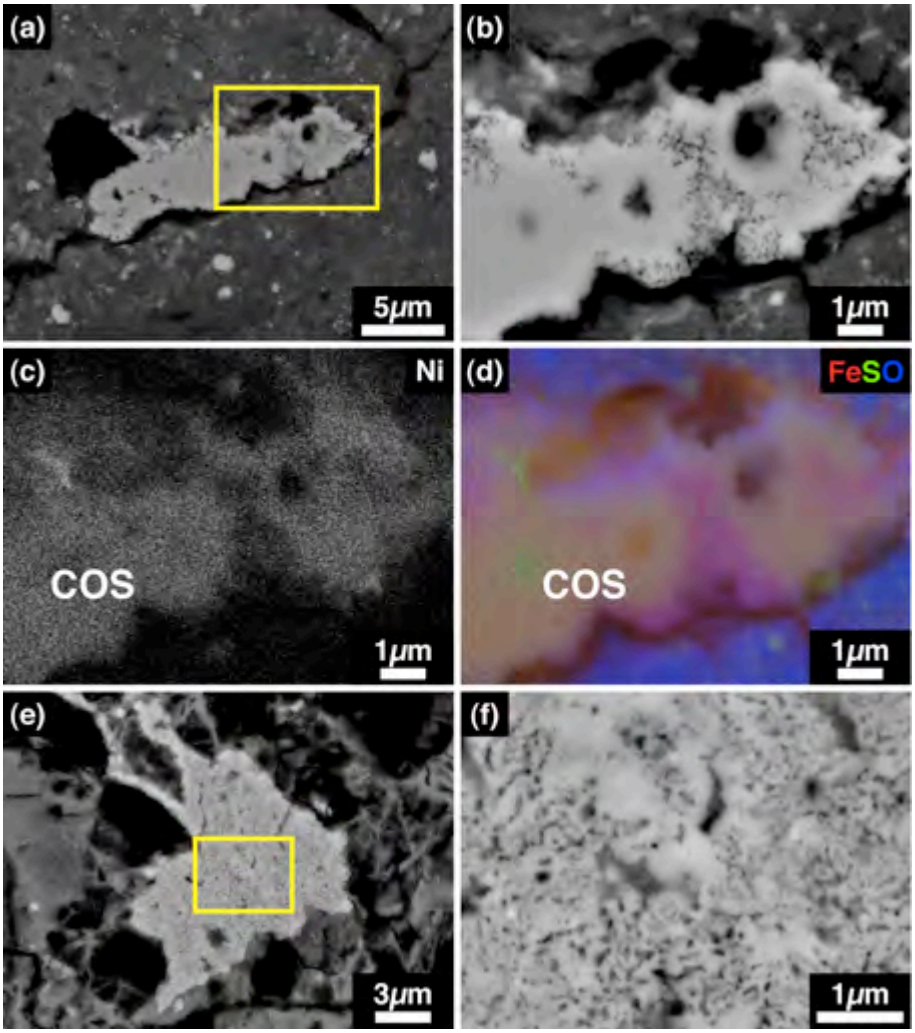

Fig. 7. (a) Backscattered electron (BSE) image of COS grain with abundant dark pores. (b) BSE image, (c) Nickel X-ray map and (d) Fe-S-O composite map of the rectangle region in (a). (e) BSE image of the COS grain having abundant dark pores for whole surface. (f) BSE image of the rectangle region in (e).

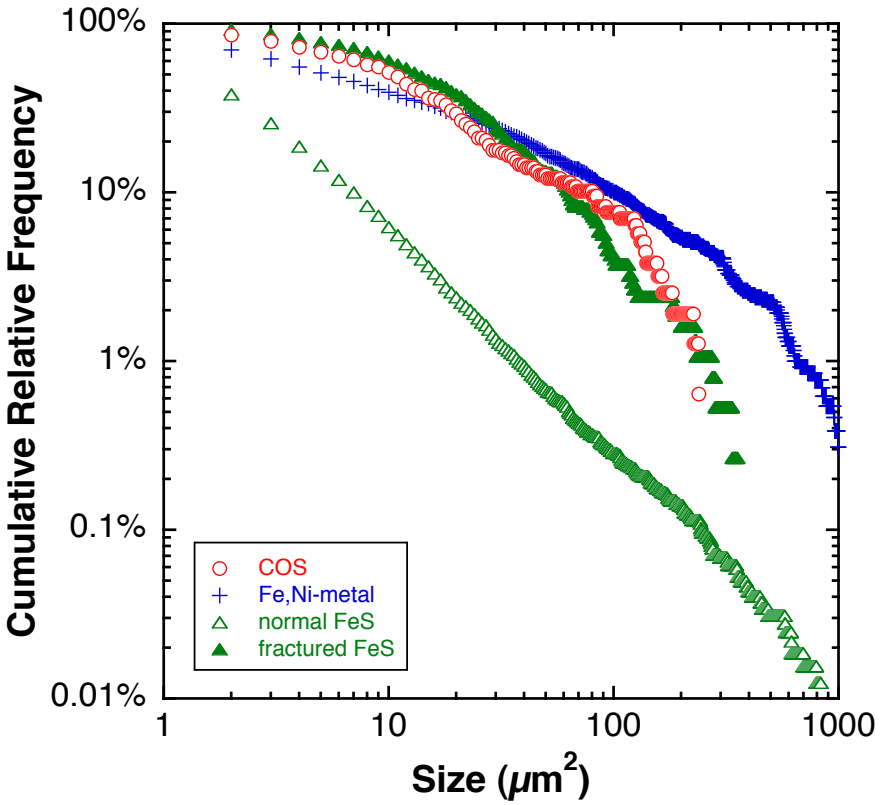

Fig. 8. Cumulative relative size distributions for COS, Fe,Ni-metal, fracture-less normal Fe,Ni-sulfide and fractured Fe,Ni-sulfide in the Acfer 094 matrix. Cumulative relative frequency is normalized to the total number of grains for each of minerals.

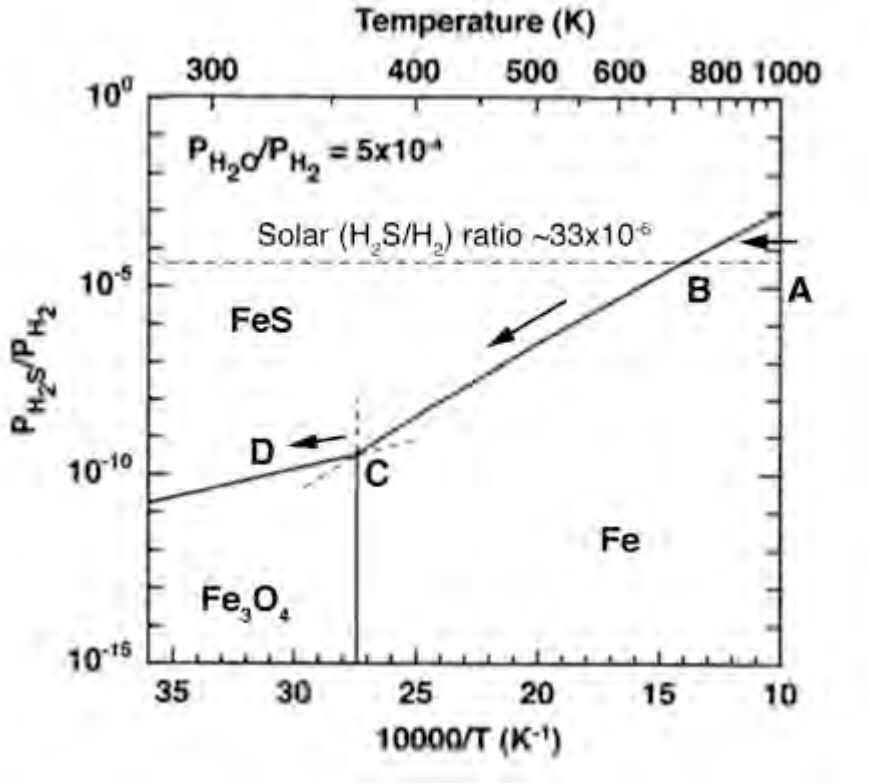

Fig. 9. Phase diagram of Fe-metal, troilite (FeS) and magnetite (Fe_3O_4) system after Sakamoto et al. (2007). Arrows indicate the path of the COS formation scenario proposed by Seto et al. (2008).

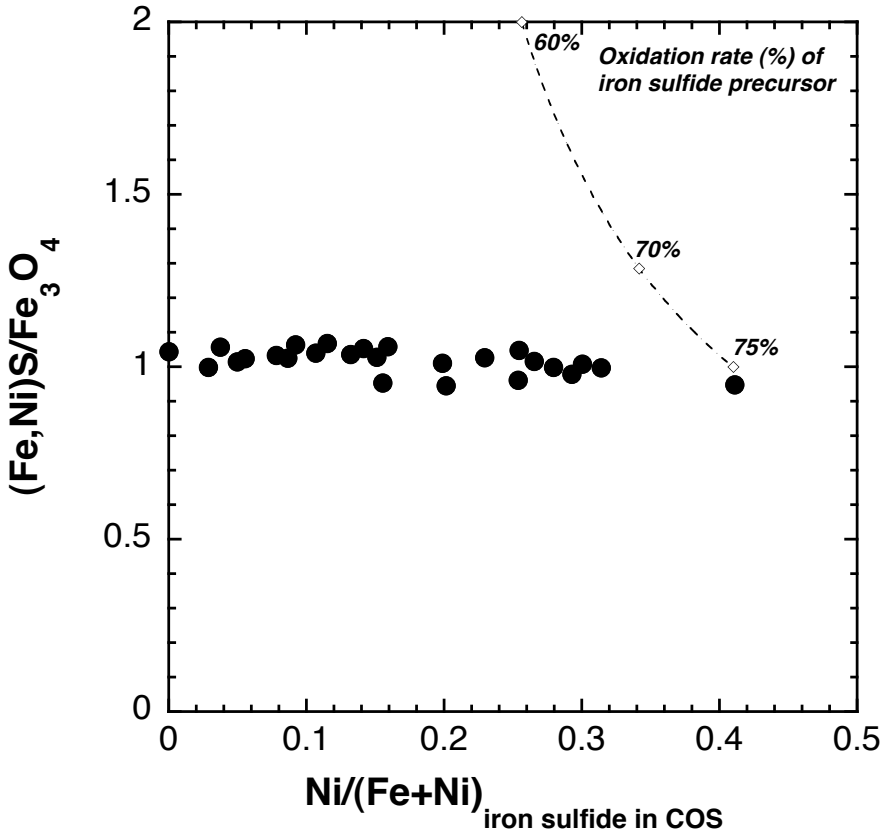

Fig. 10. Relationship between ratios of iron sulfide to magnetite of COS and Ni contents of iron sulfide in COS. When troilite was oxidized to form magnetite, iron sulfide/magnetite ratio of COS may vary along a dashed line in the figure depending on the oxidation rate of iron sulfide precursor.

APPENDIX

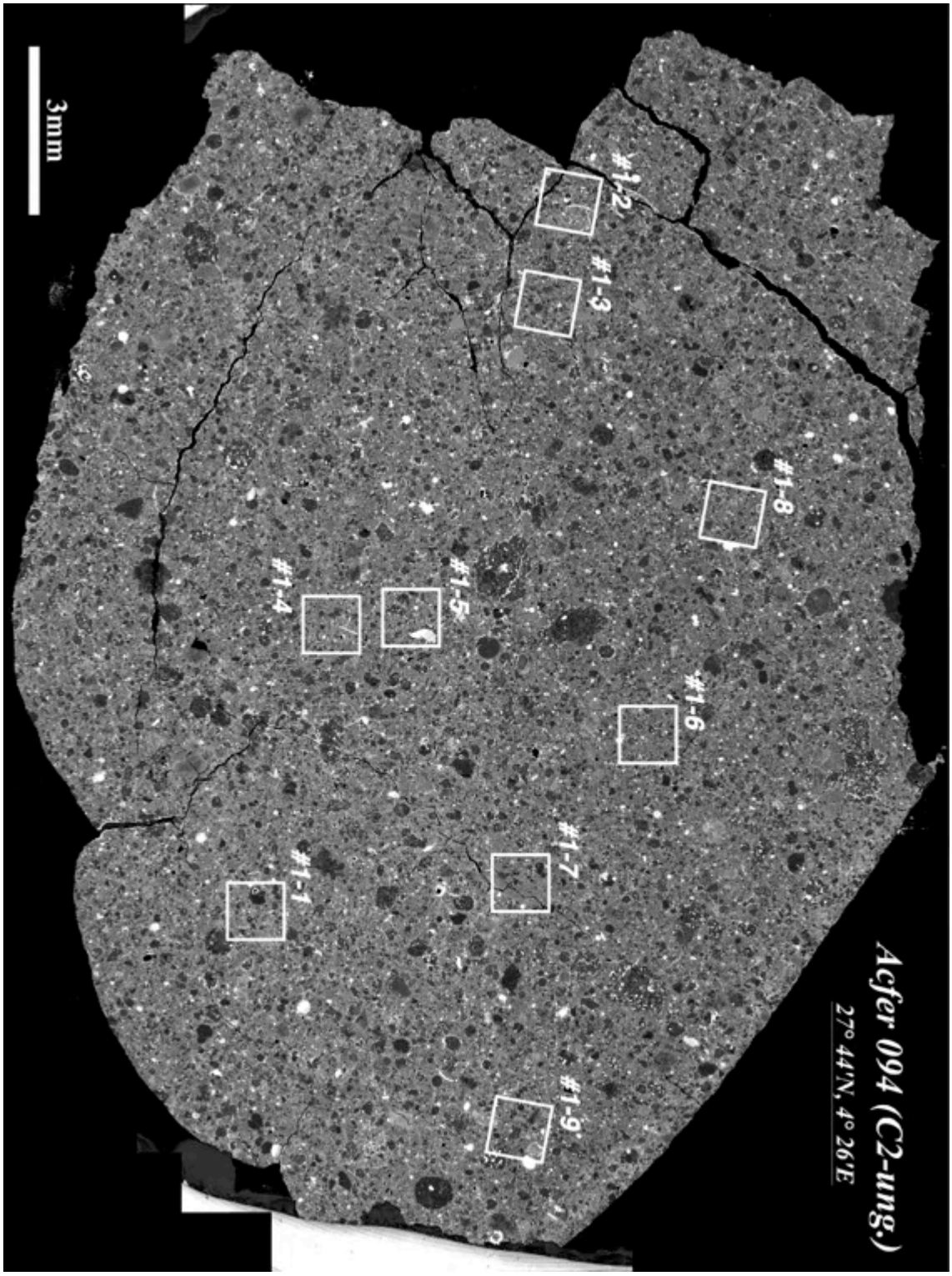

Fig. 11. Backscattered electron image of the entire thin section of Acfer 094#1. White squares correspond to the X-ray elemental mapped regions of a 1×1 mm area.

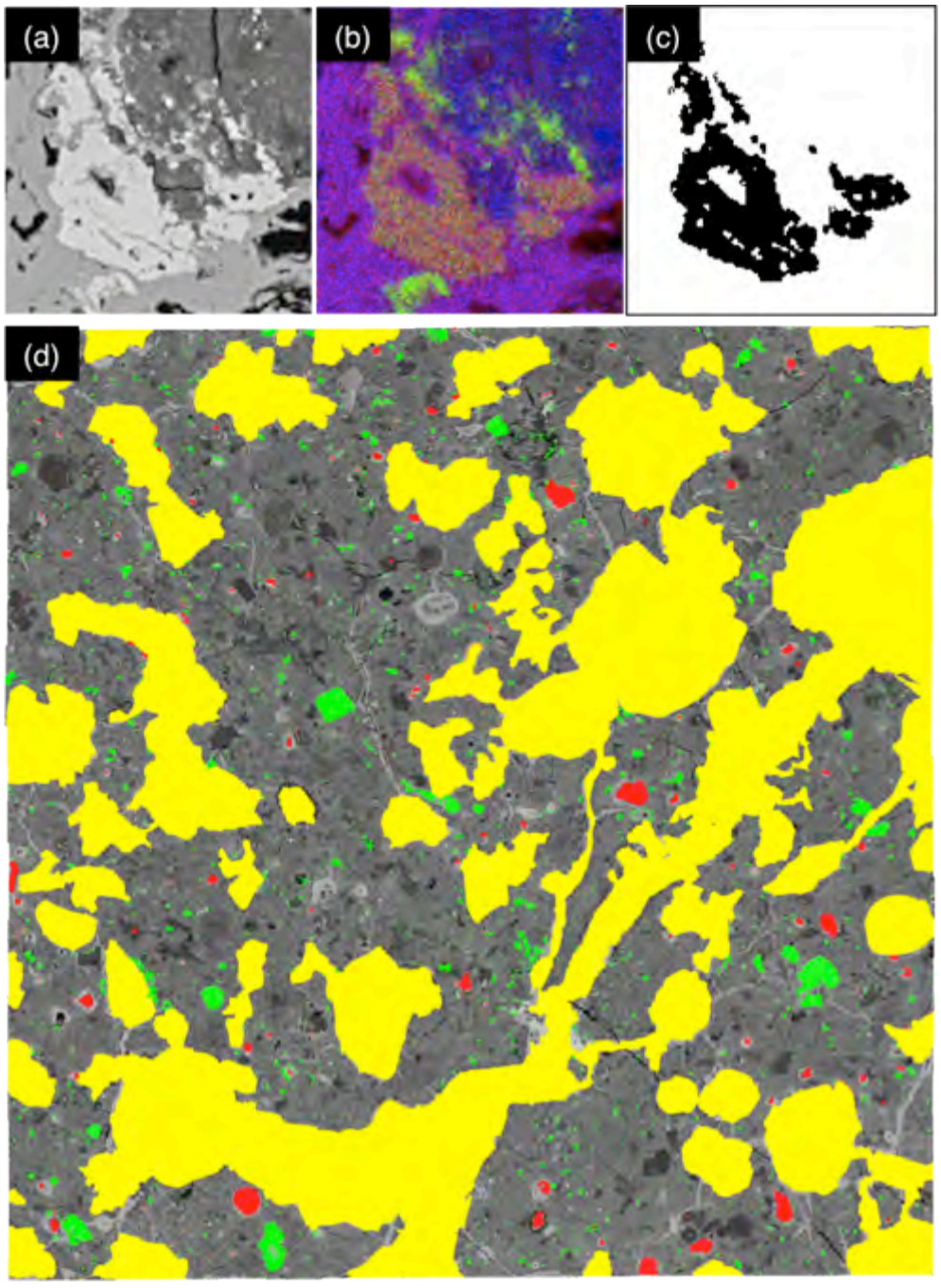

Fig. 12. Procedure of image analysis. (a) Backscattered electron image (b) Fe-S-O composite map (c) masked map of a COS grain. (d) Mineral masks overlaid on backscattered electron image of Acfer 094#2-2. Red and green areas show Fe,Ni-metal and sulfide, respectively. Non-matrix areas (grains >50 μm in diameter) are masked as yellow color.

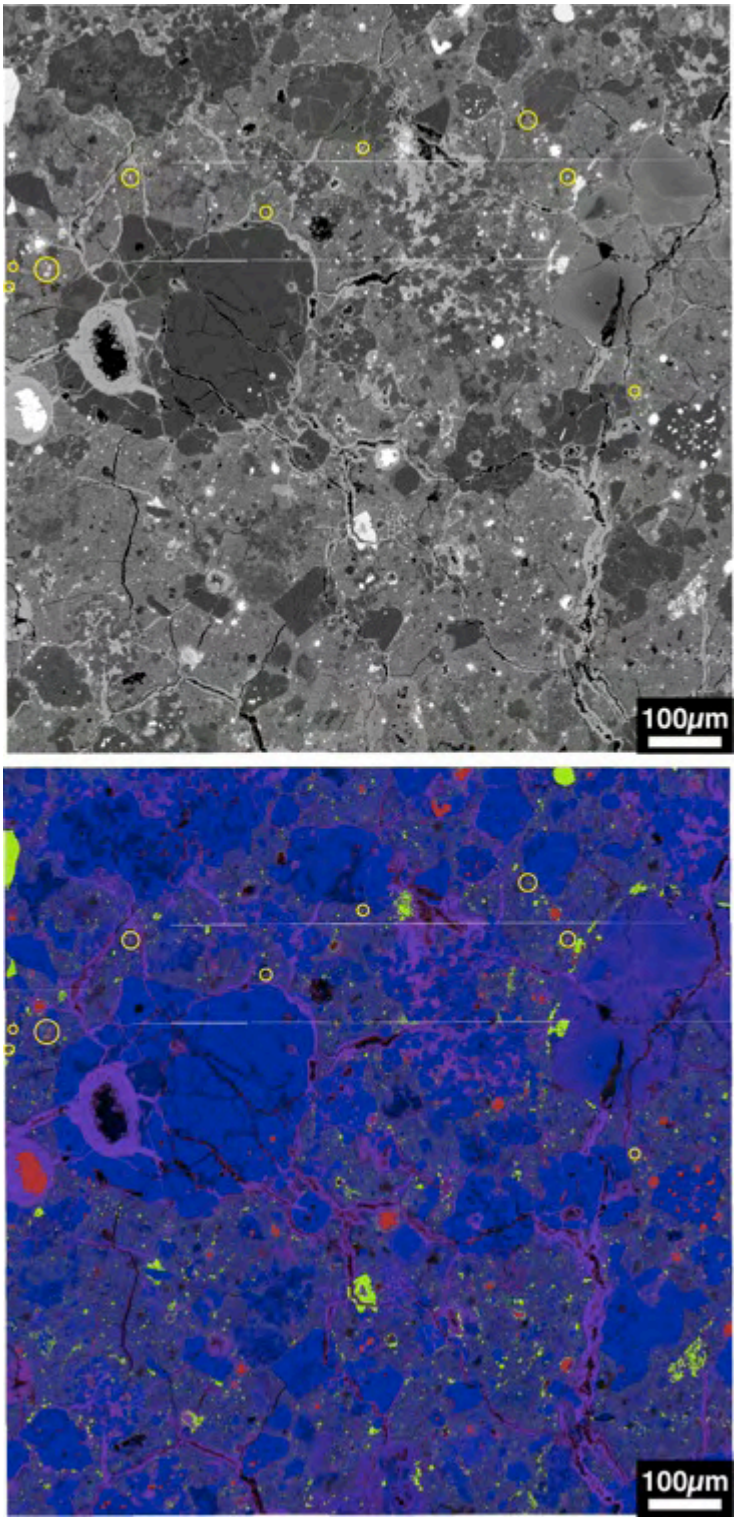

Fig. 13. Backscattered electron image and Fe-S-O map of Acfer 094#1-1. Yellow circles show the positions of COS grains.

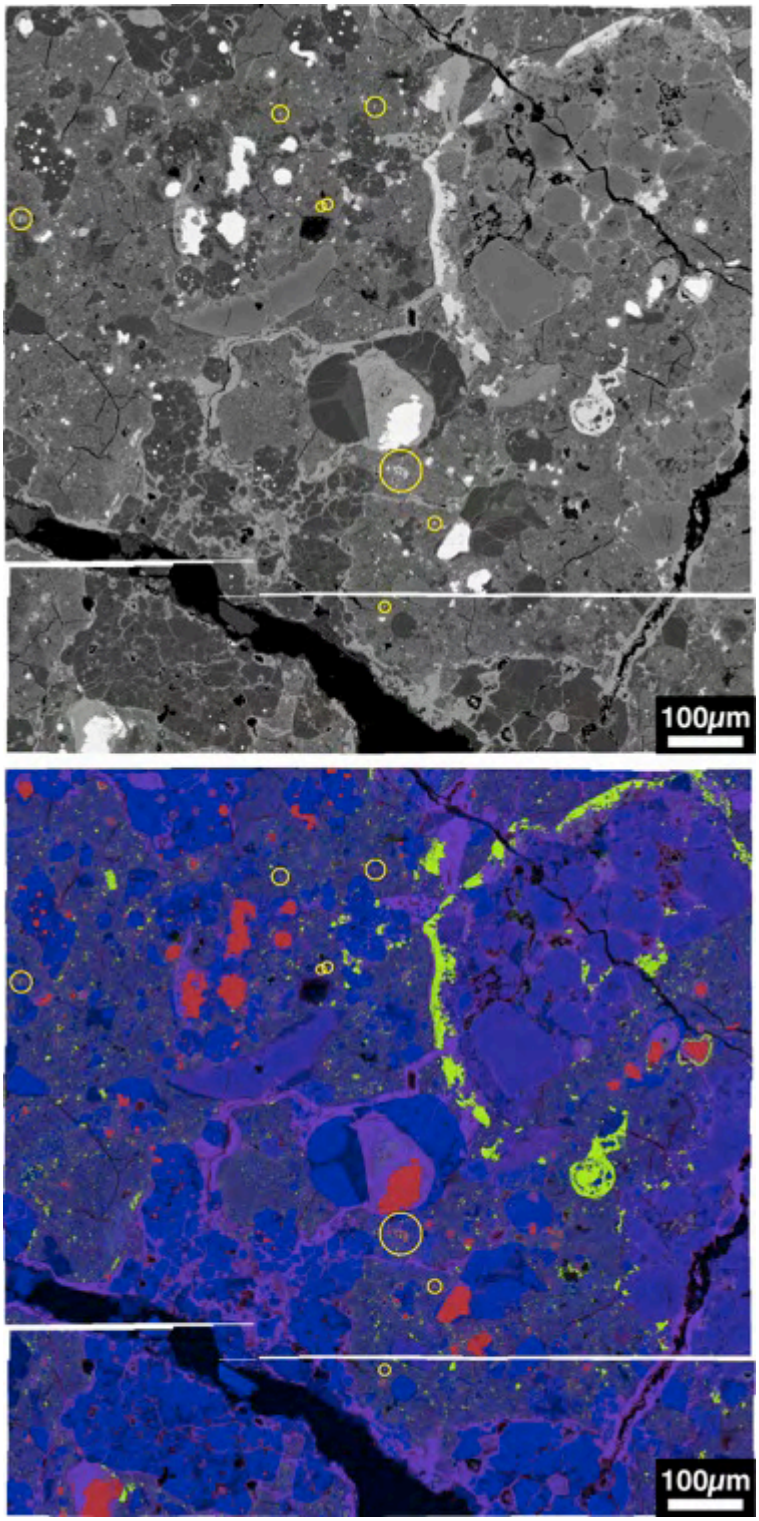

Fig. 14. Backscattered electron image and Fe-S-O map of Acfer 094#1-2. Yellow circles show the positions of COS grains.

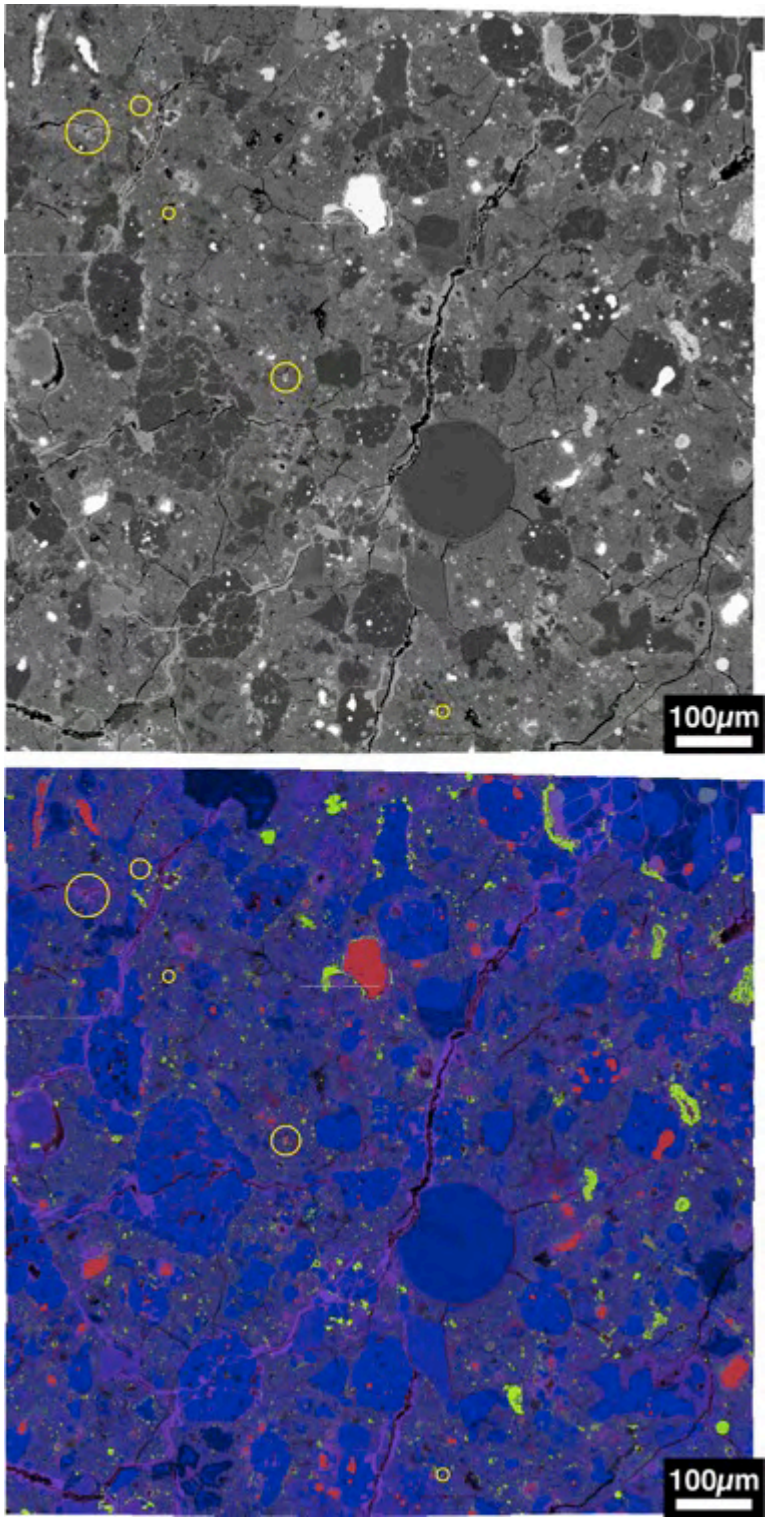

Fig. 15. Backscattered electron image and Fe-S-O map of Acfer 094#1-3. Yellow circles show the positions of COS grains.

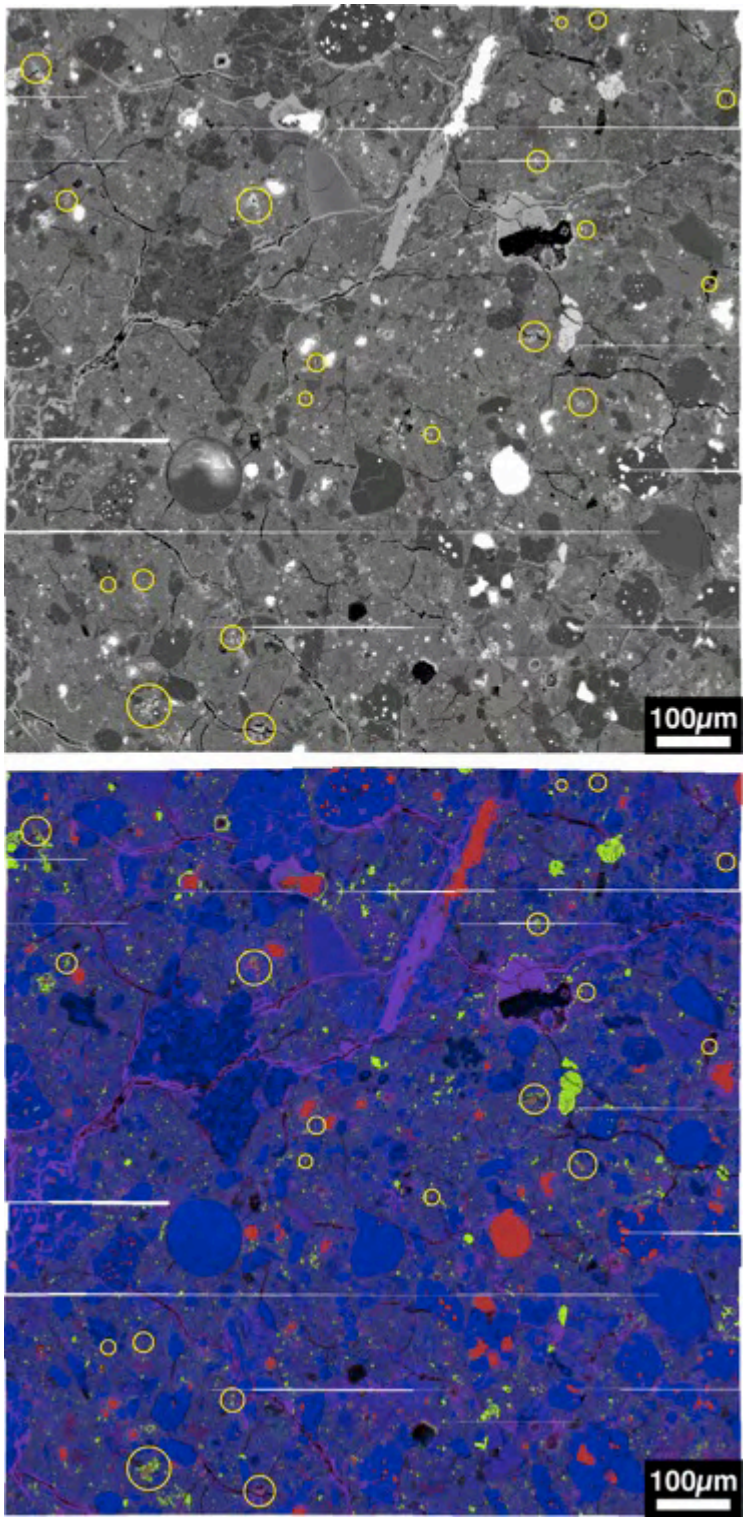

Fig. 16. Backscattered electron image and Fe-S-O map of Acfer 094#1-4. Yellow circles show the positions of COS grains.

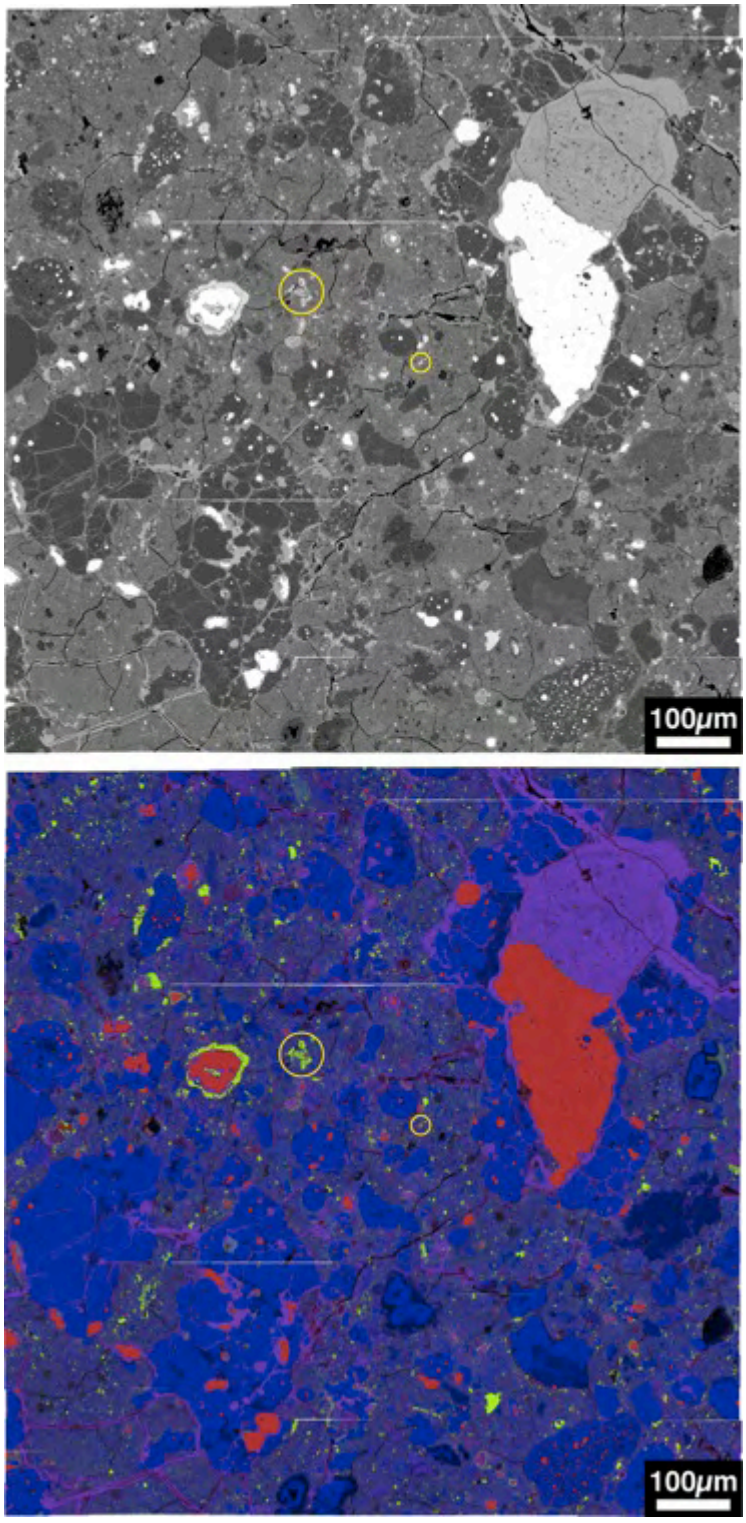

Fig. 17. Backscattered electron image and Fe-S-O map of Acfer 094#1-5. Yellow circles show the positions of COS grains.

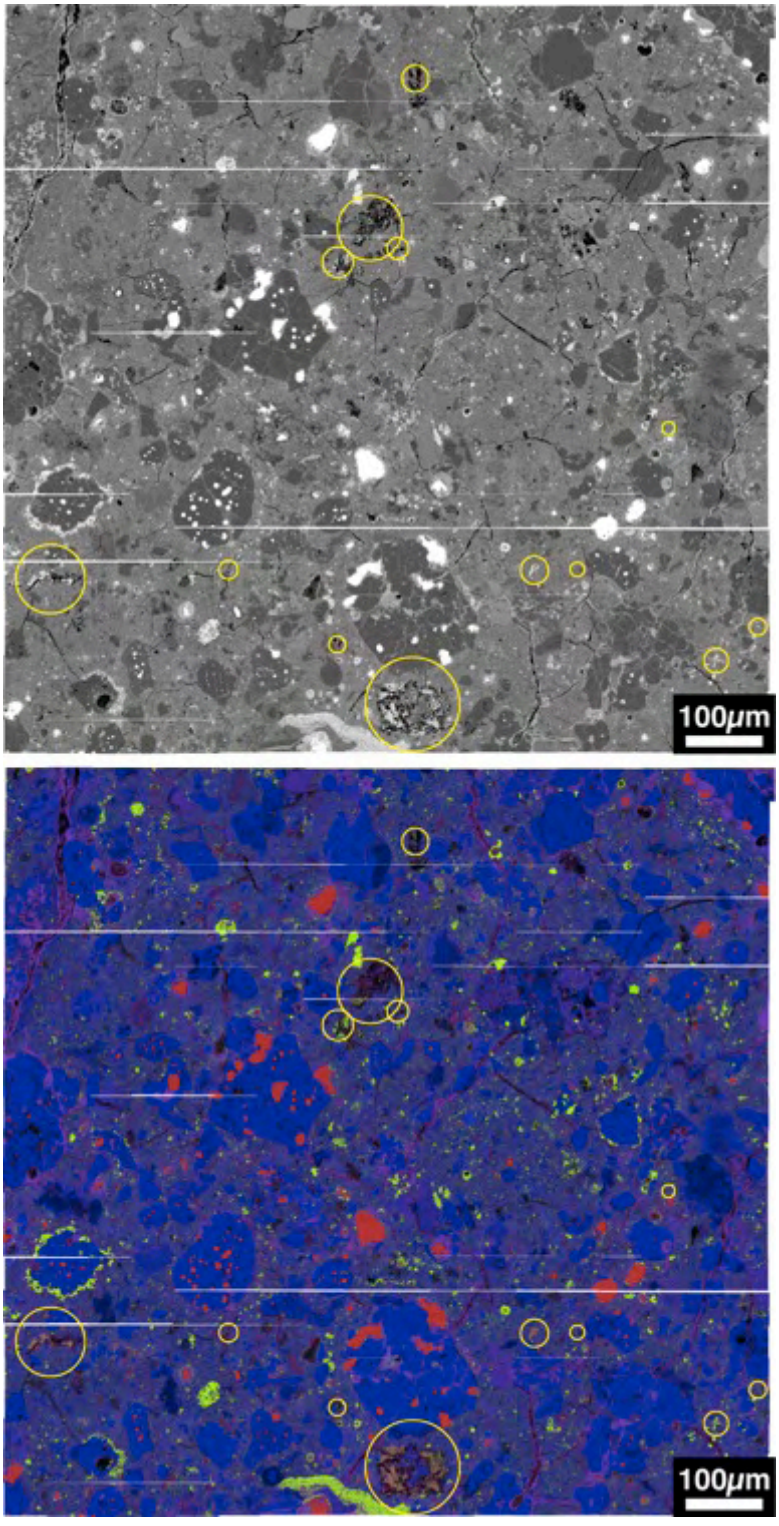

Fig. 18. Backscattered electron image and Fe-S-O map of Acfer 094#1-6. Yellow circles show the positions of COS grains.

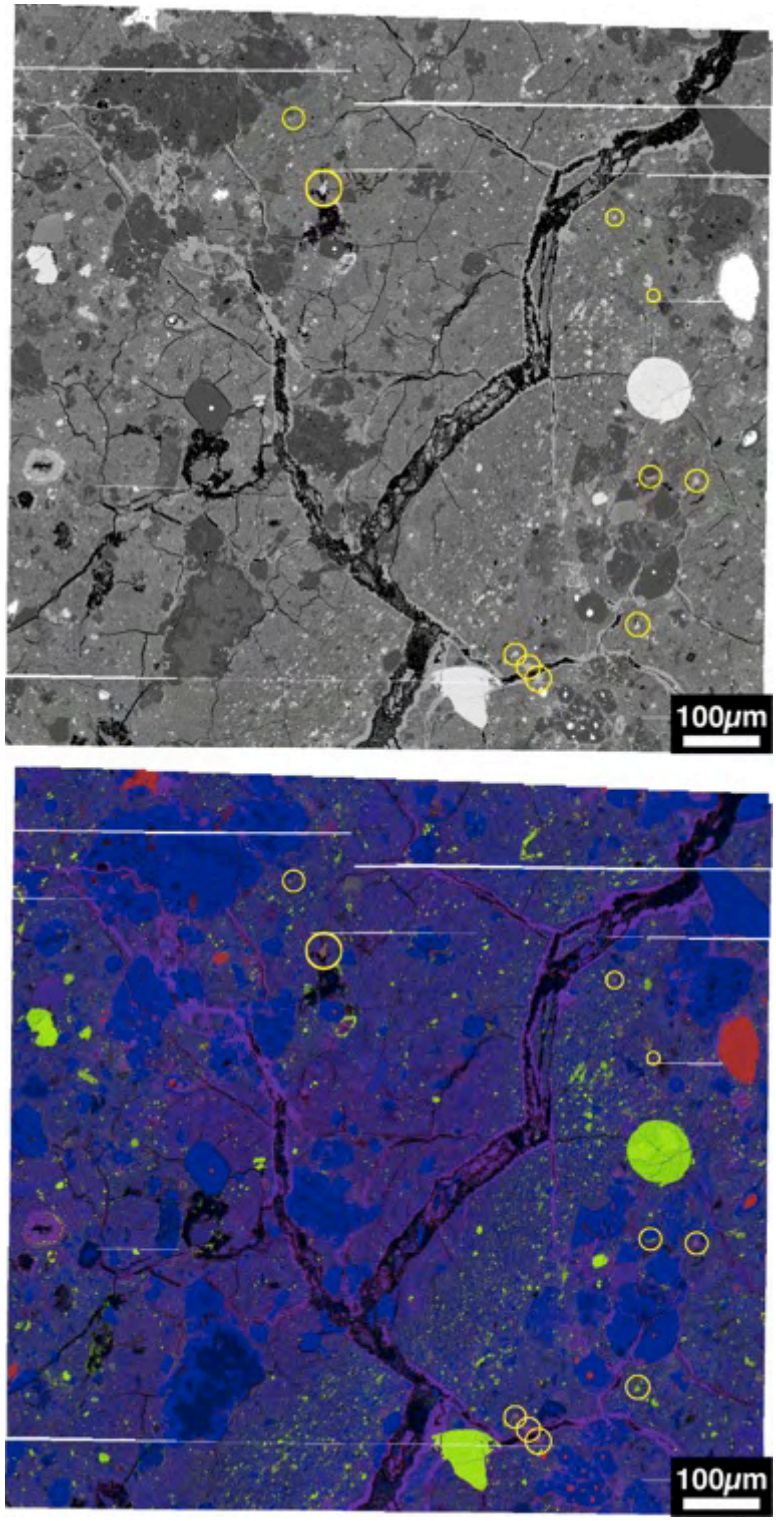

Fig. 19. Backscattered electron image and Fe-S-O map of Acfer 094#1-7. Yellow circles show the positions of COS grains.

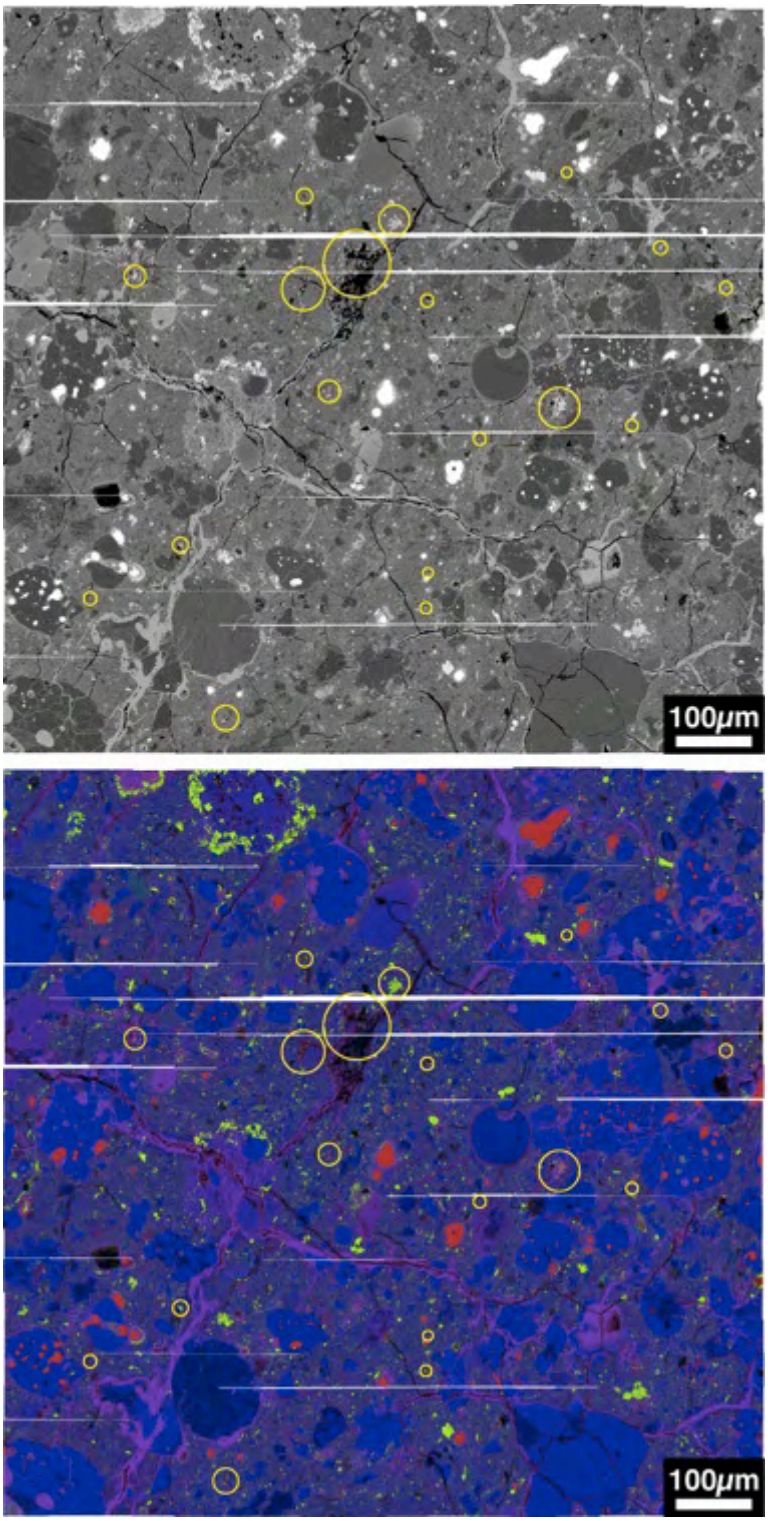

Fig. 20. Backscattered electron image and Fe-S-O map of Acfer 094#1-8. Yellow circles show the positions of COS grains.

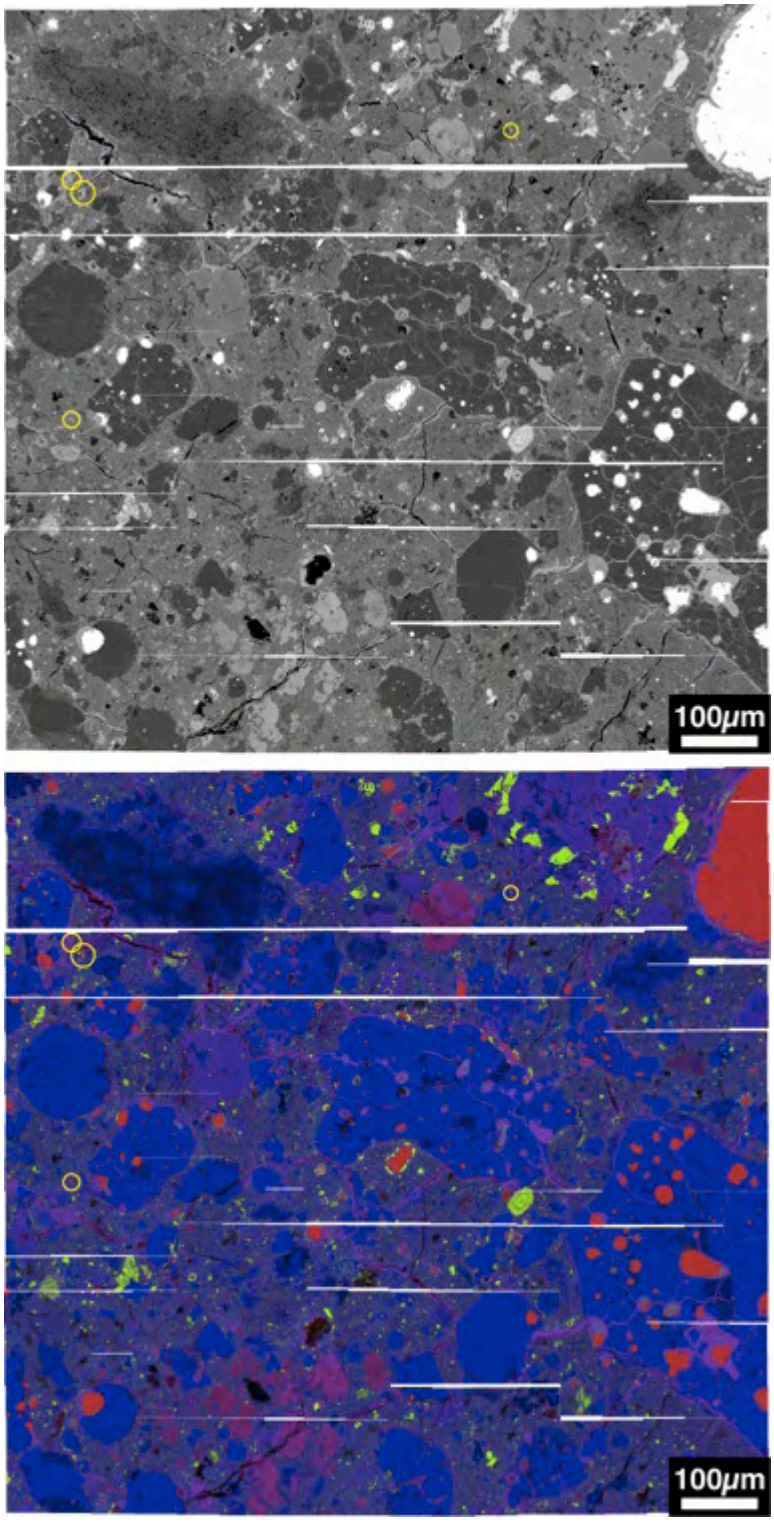

Fig. 21. Backscattered electron image and Fe-S-O map of Acfer 094#1-9. Yellow circles show the positions of COS grains.

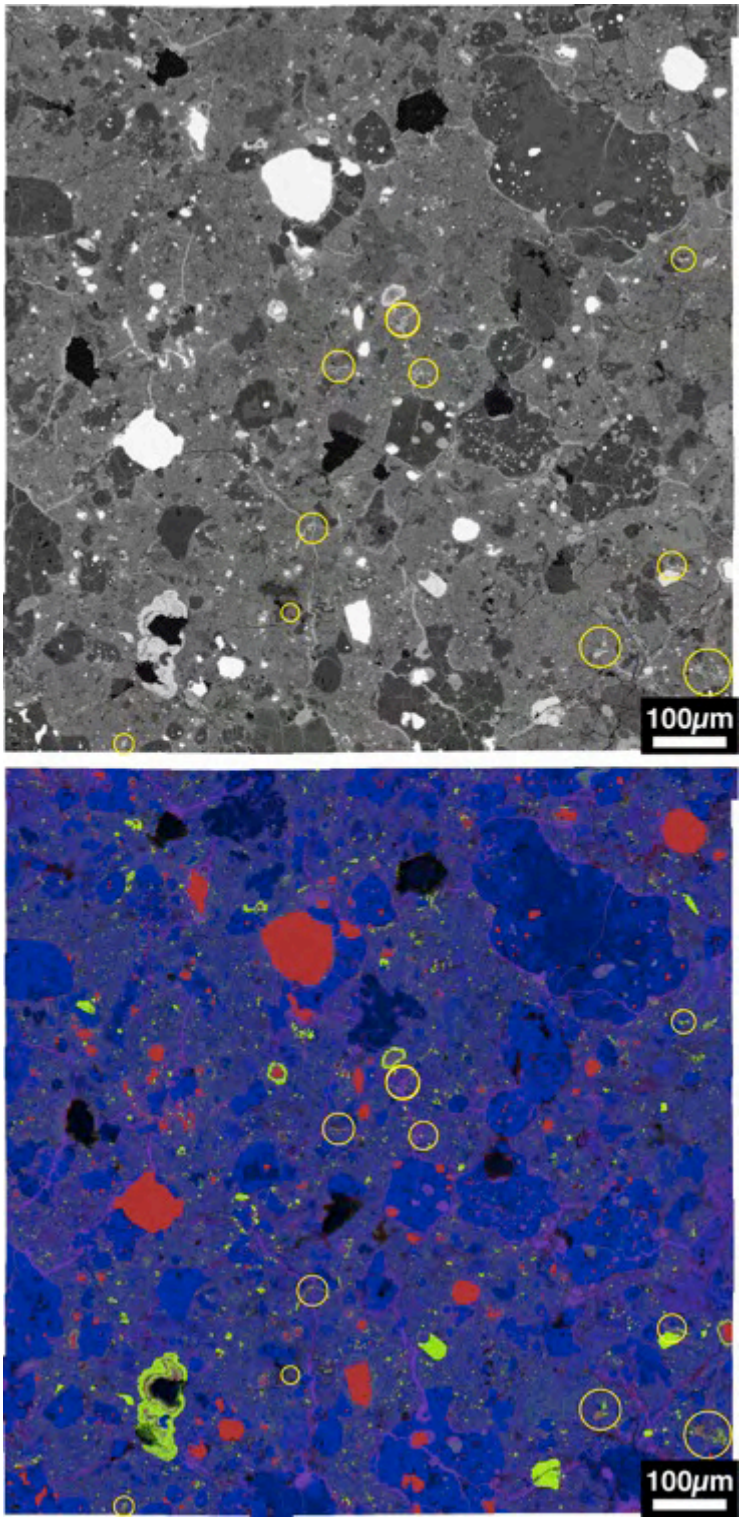

Fig. 22. Backscattered electron image and Fe-S-O map of Acfer 094#2-1. Yellow circles show the positions of COS grains.

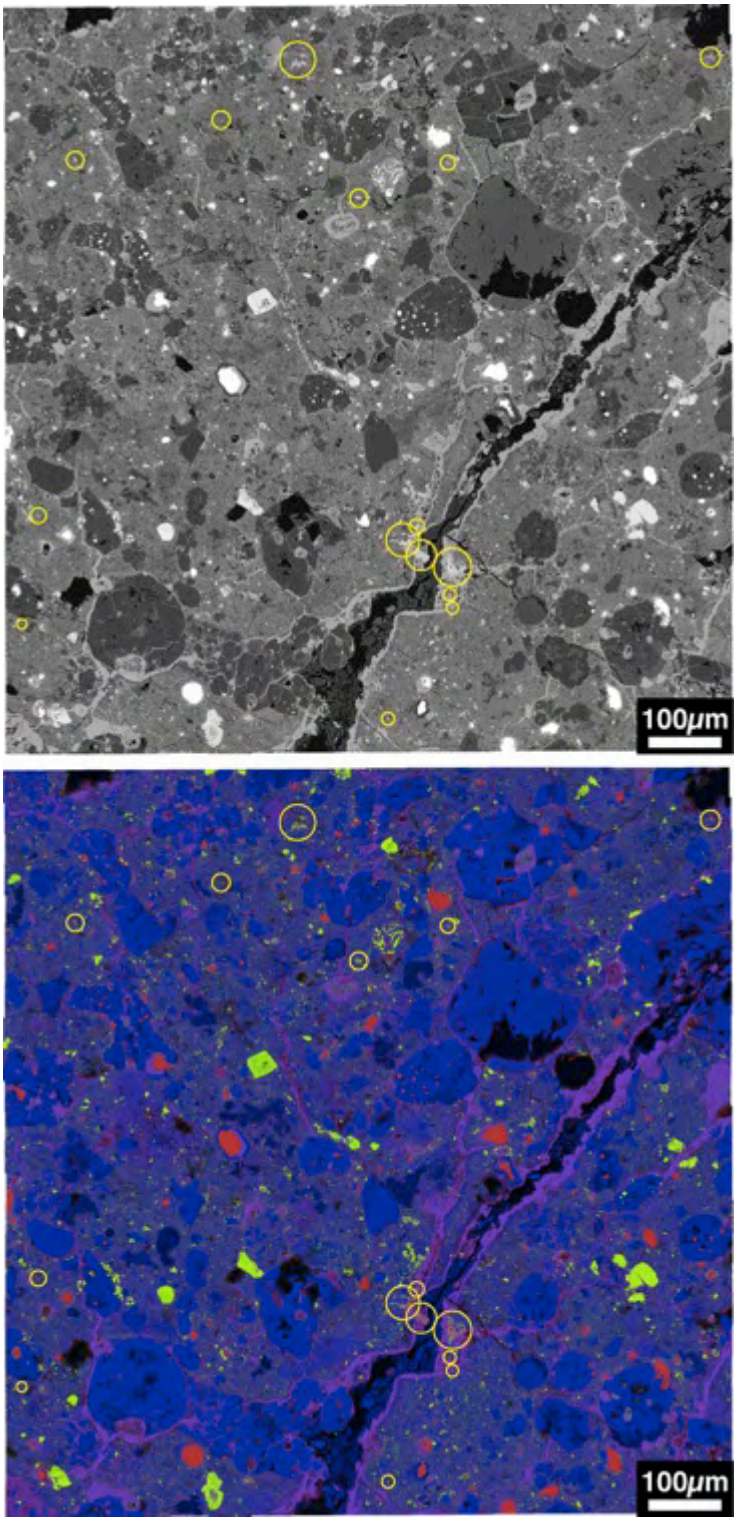

Fig. 23. Backscattered electron image and Fe-S-O map of Acfer 094#2-2. Yellow circles show the positions of COS grains.

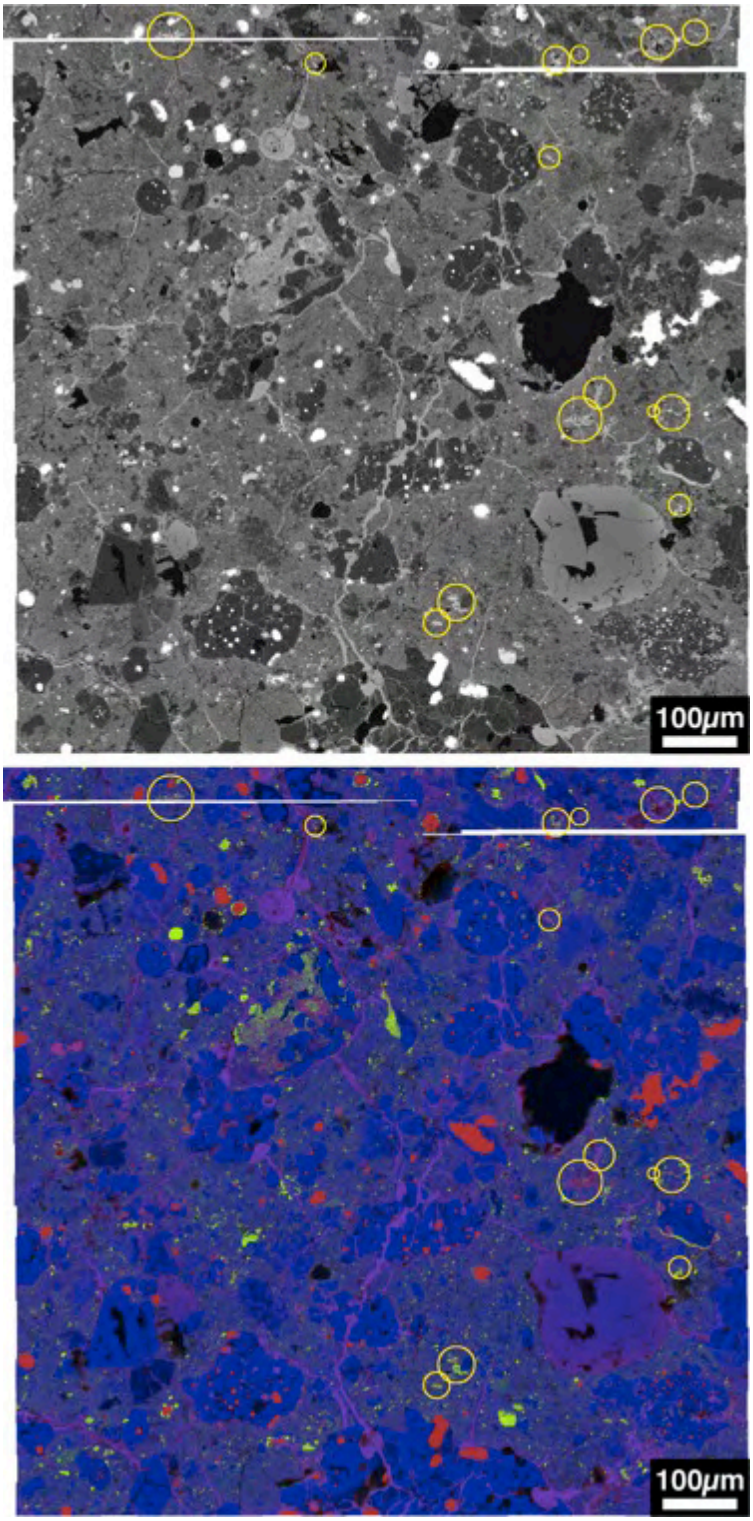

Fig. 24. Backscattered electron image and Fe-S-O map of Acfer 094#2-3. Yellow circles show the positions of COS grains.

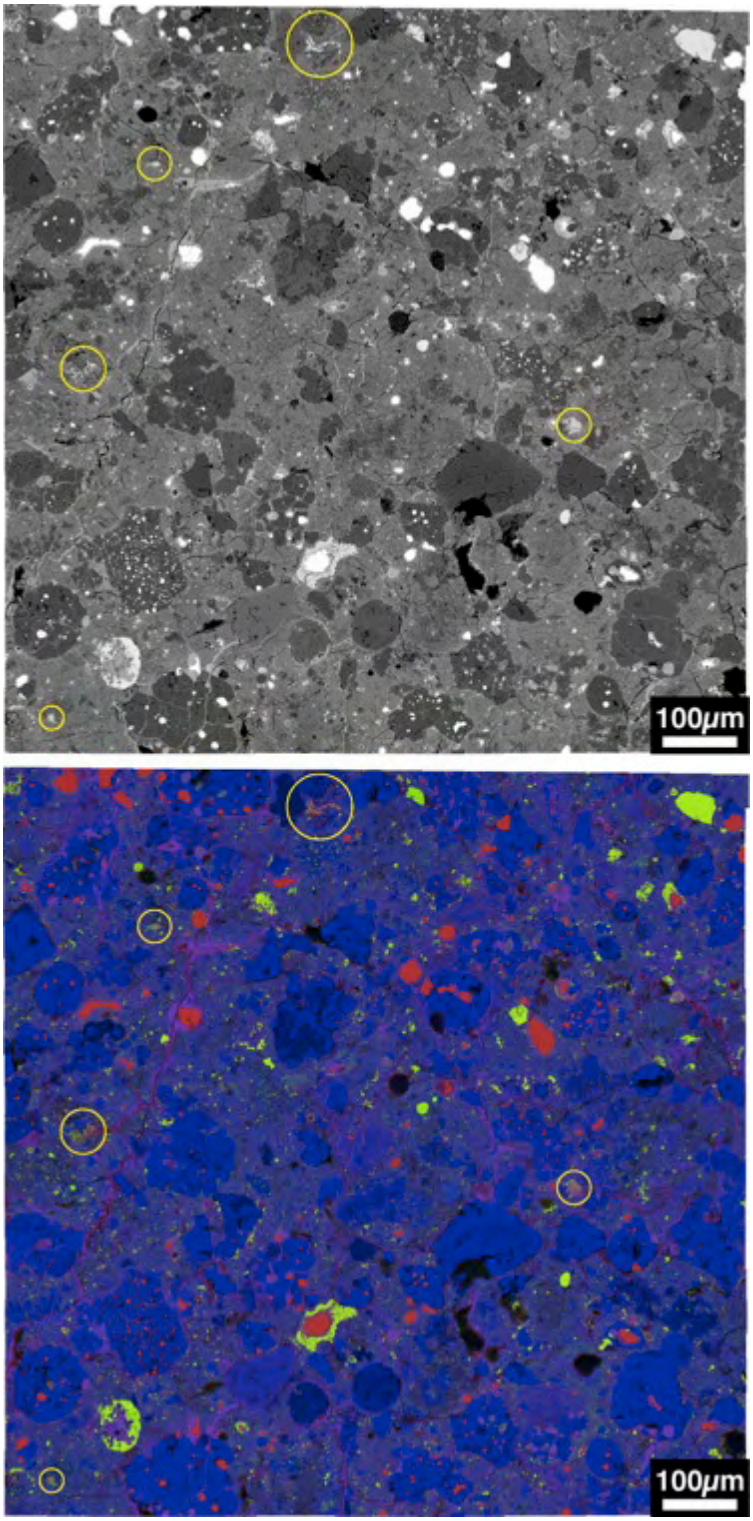

Fig. 25. Backscattered electron image and Fe-S-O map of Acfer 094#2-4. Yellow circles show the positions of COS grains.

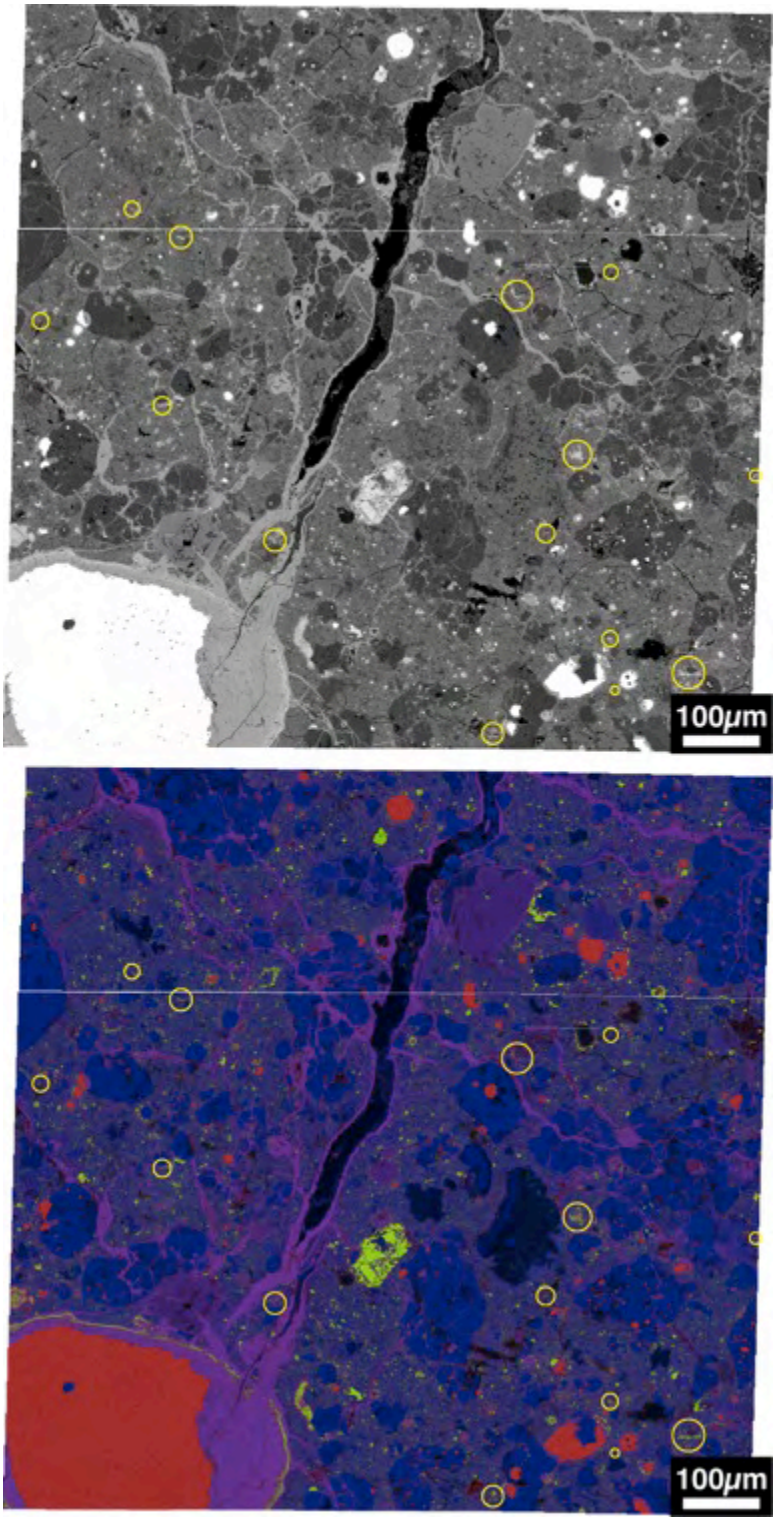

Fig. 26. Backscattered electron image and Fe-S-O map of Acfer 094#2-5. Yellow circles show the positions of COS grains.

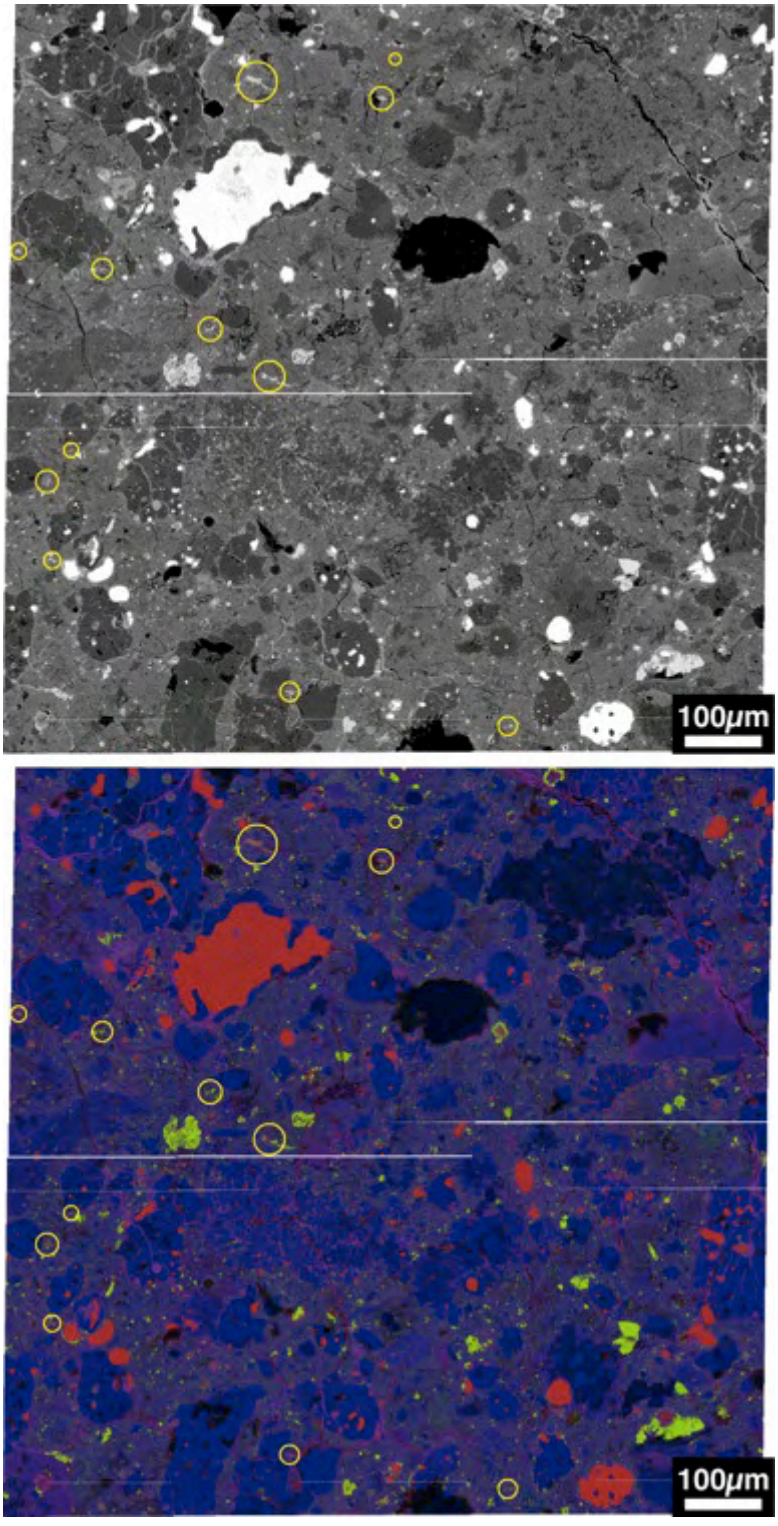

Fig. 27. Backscattered electron image and Fe-S-O map of Acfer 094#2-6. Yellow circles show the positions of COS grains.

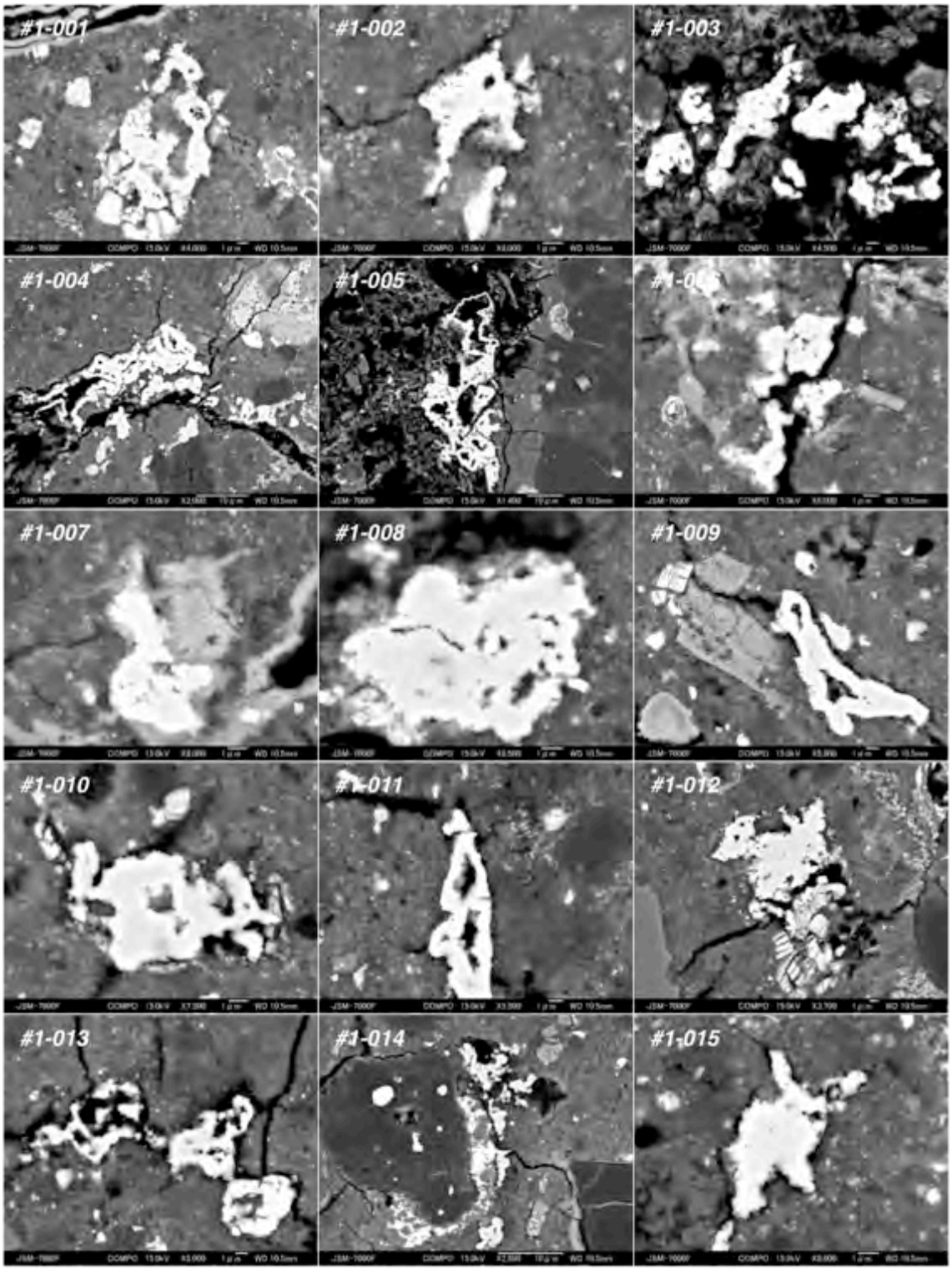

Fig. 28. Backscattered electron images of all COS grains in this study.

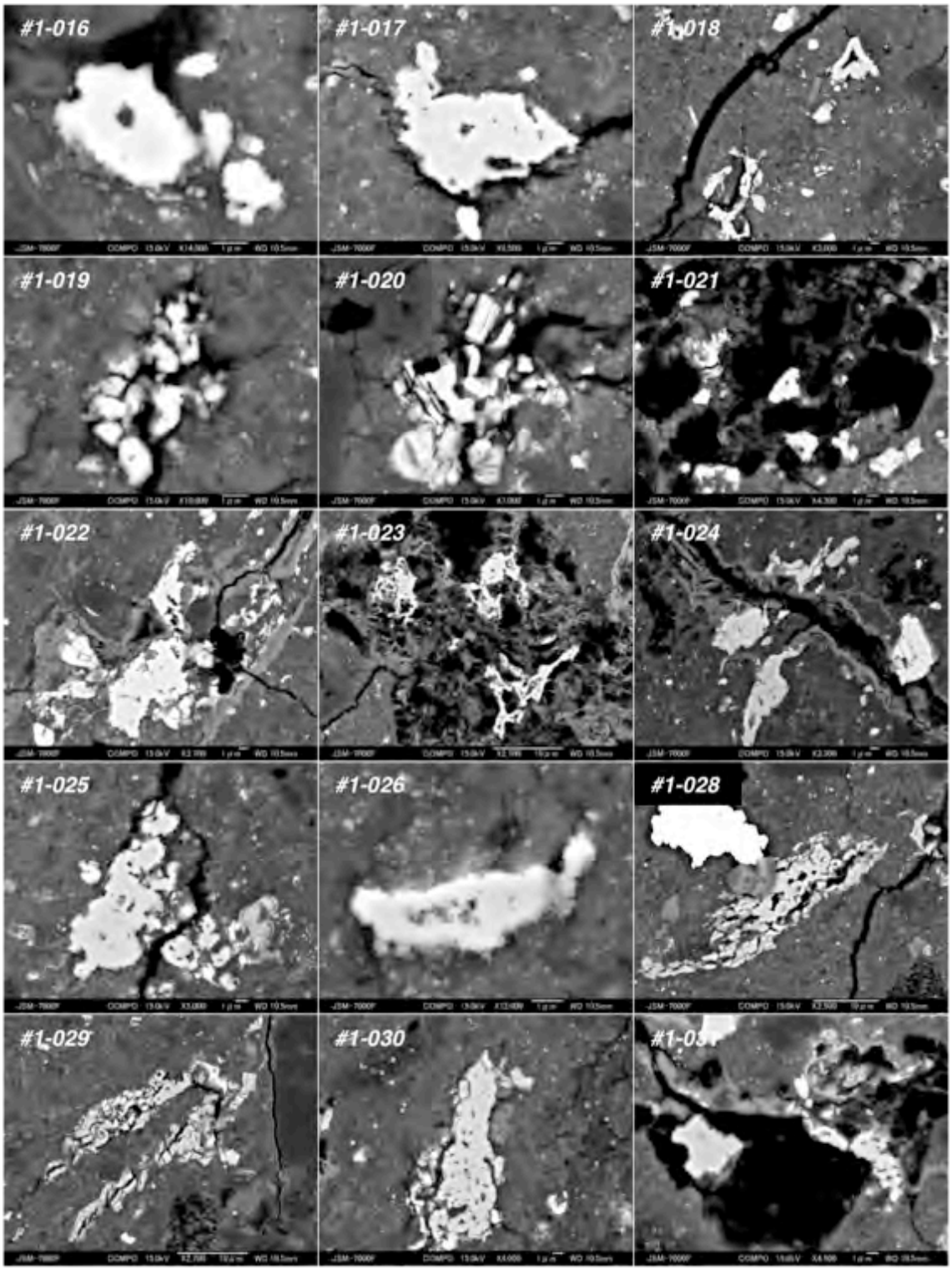

Fig. 28. (continued)

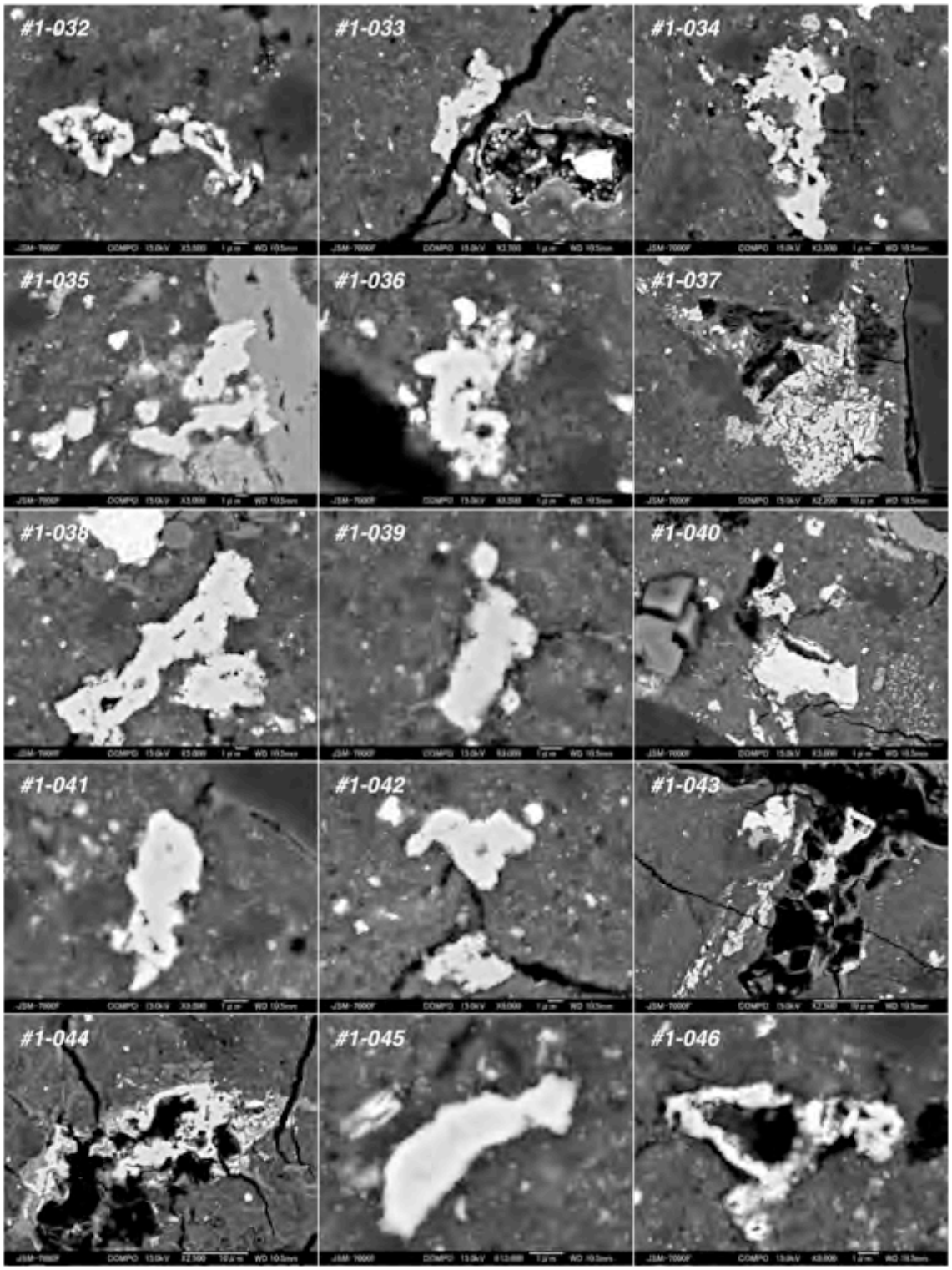

Fig. 28. (continued)

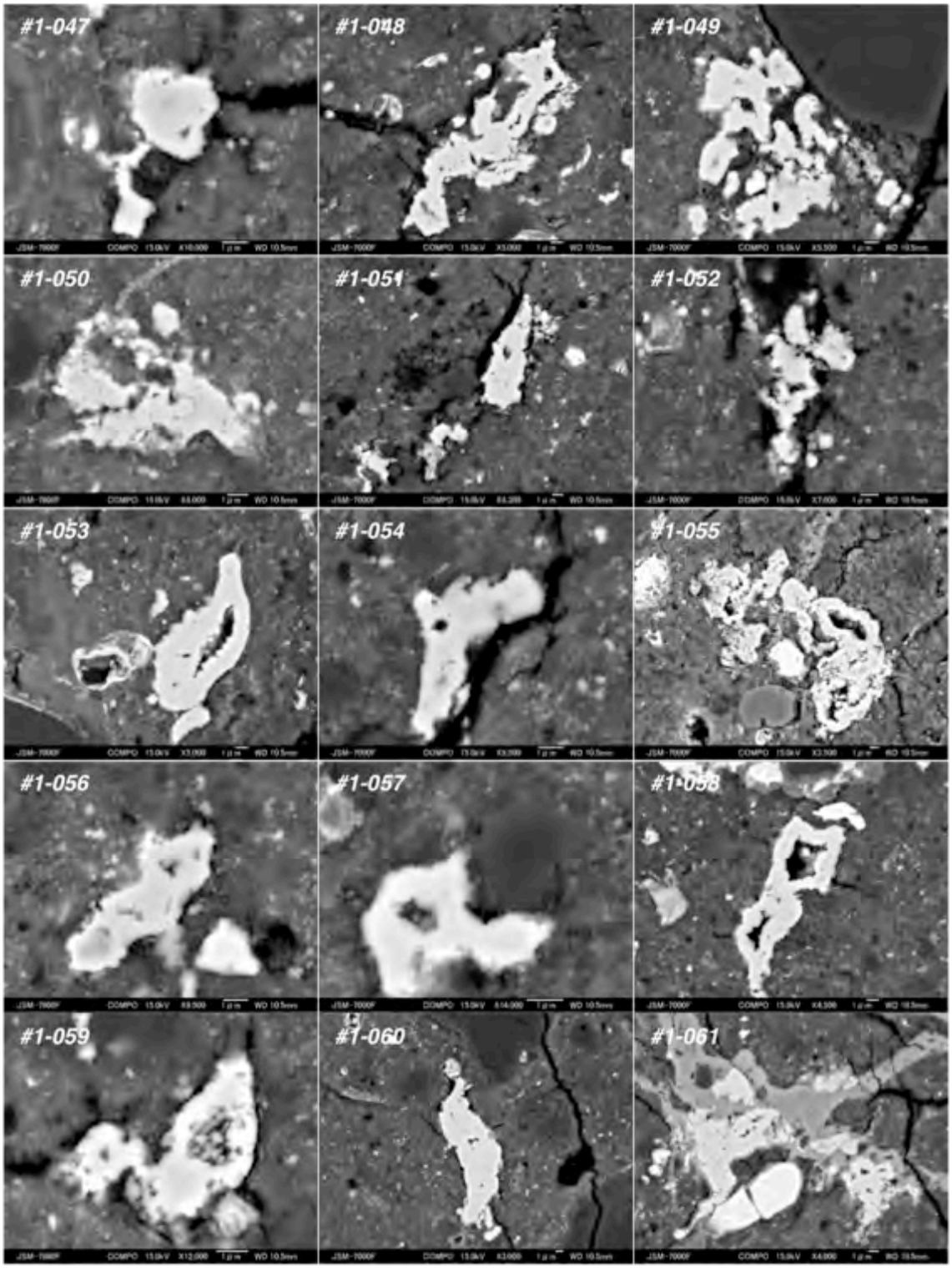

Fig. 28. (continued)

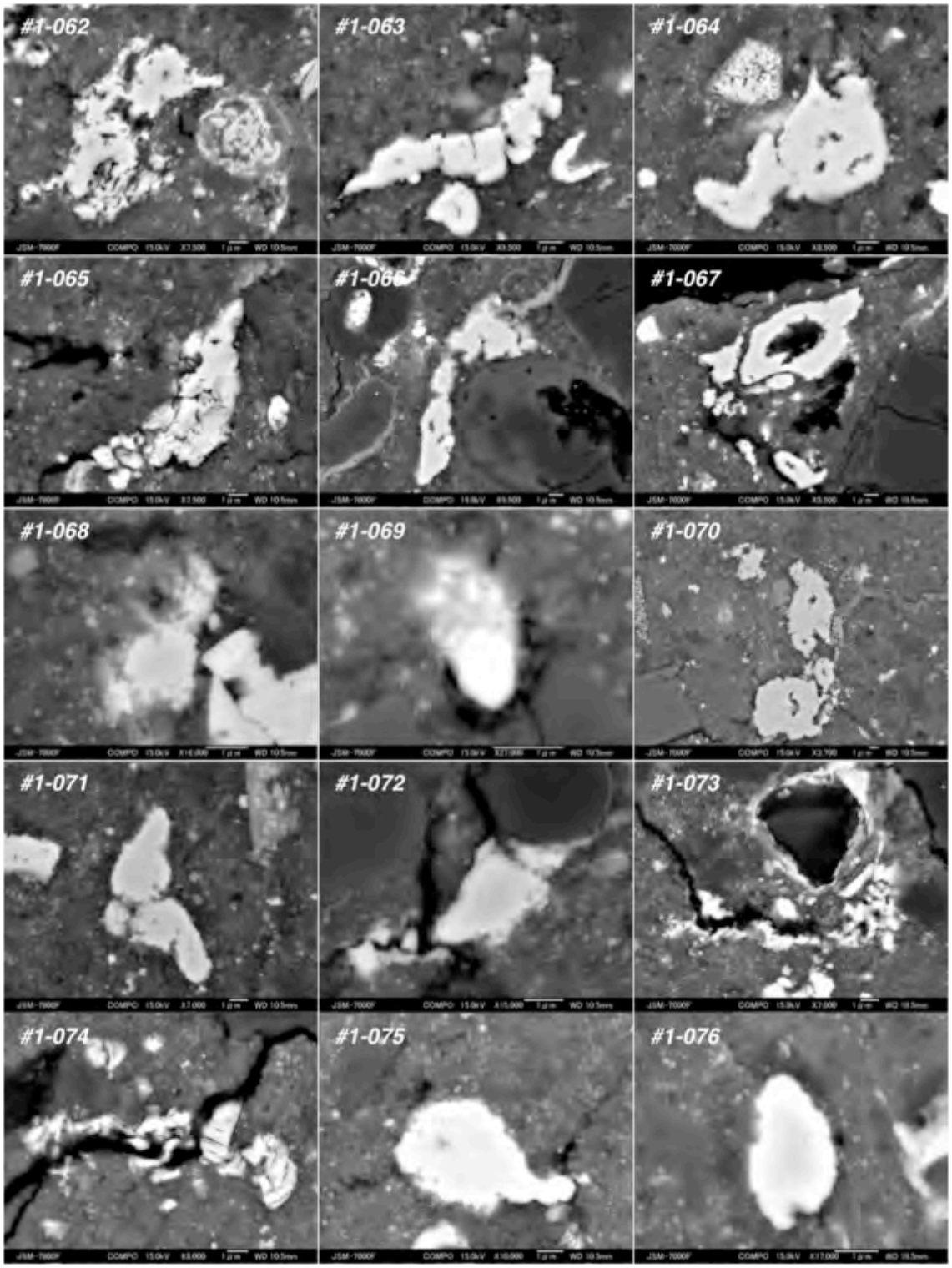

Fig. 28. (continued)

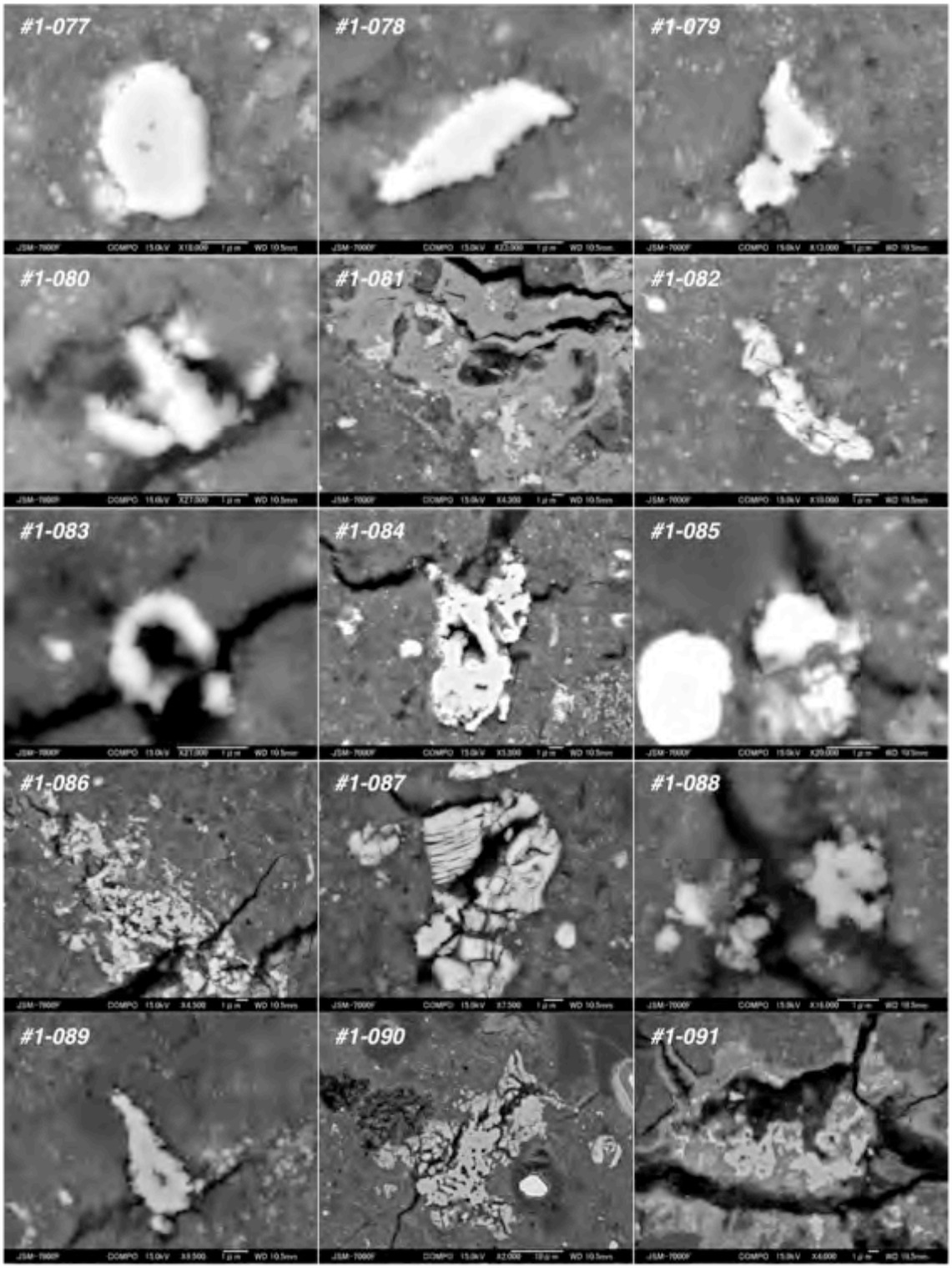

Fig. 28. (continued)

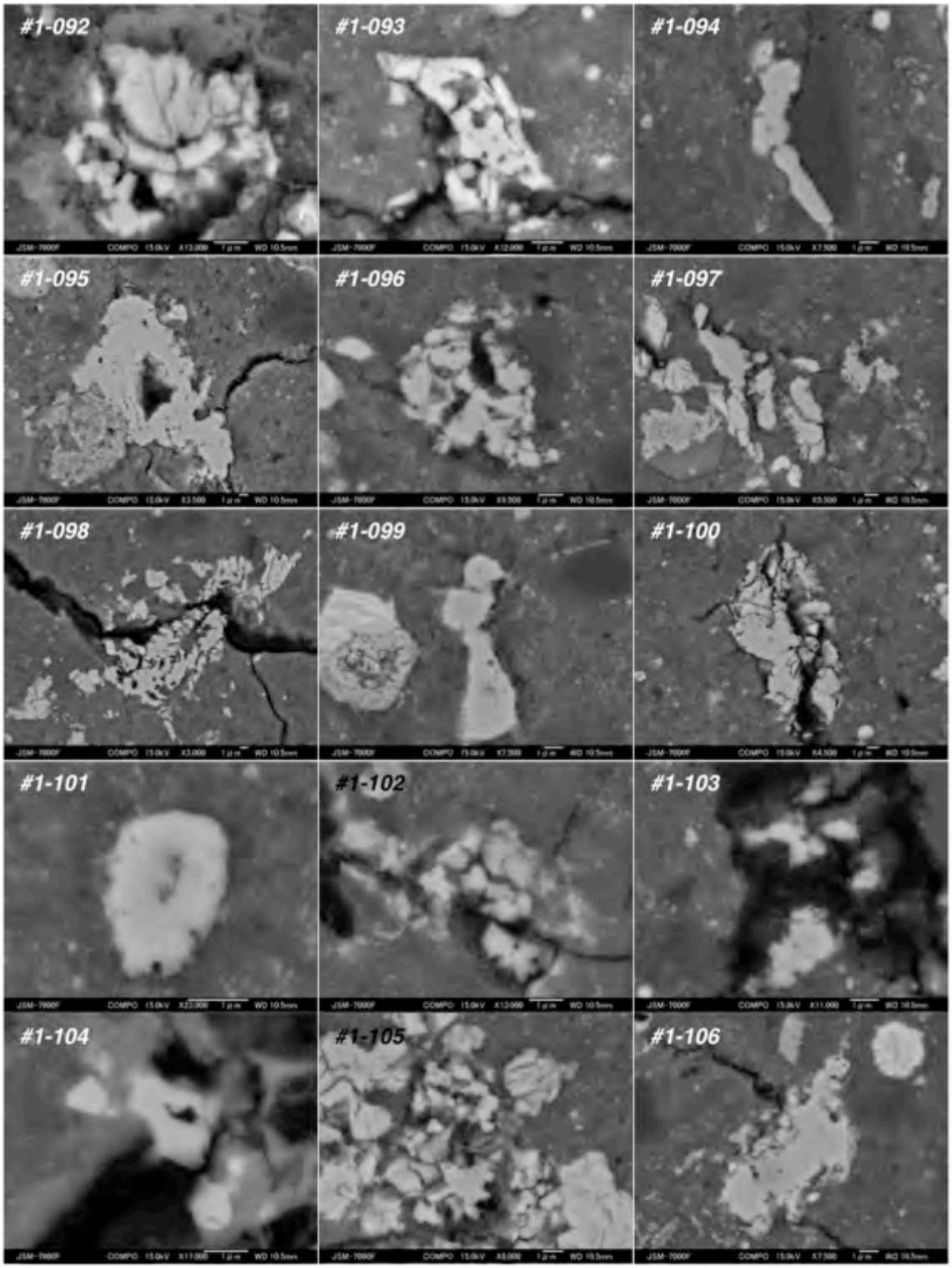

Fig. 28. (continued)

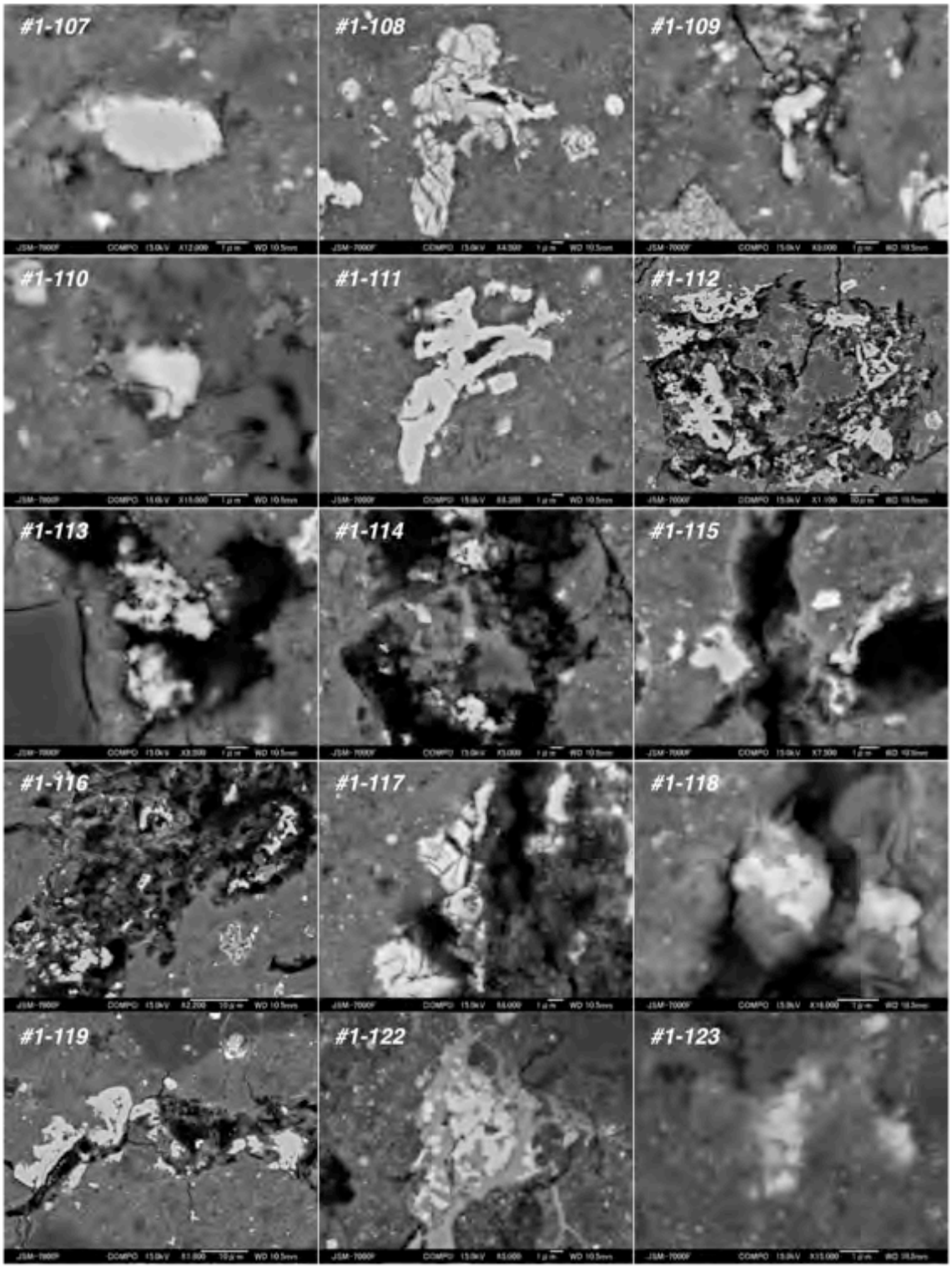

Fig. 28. (continued)

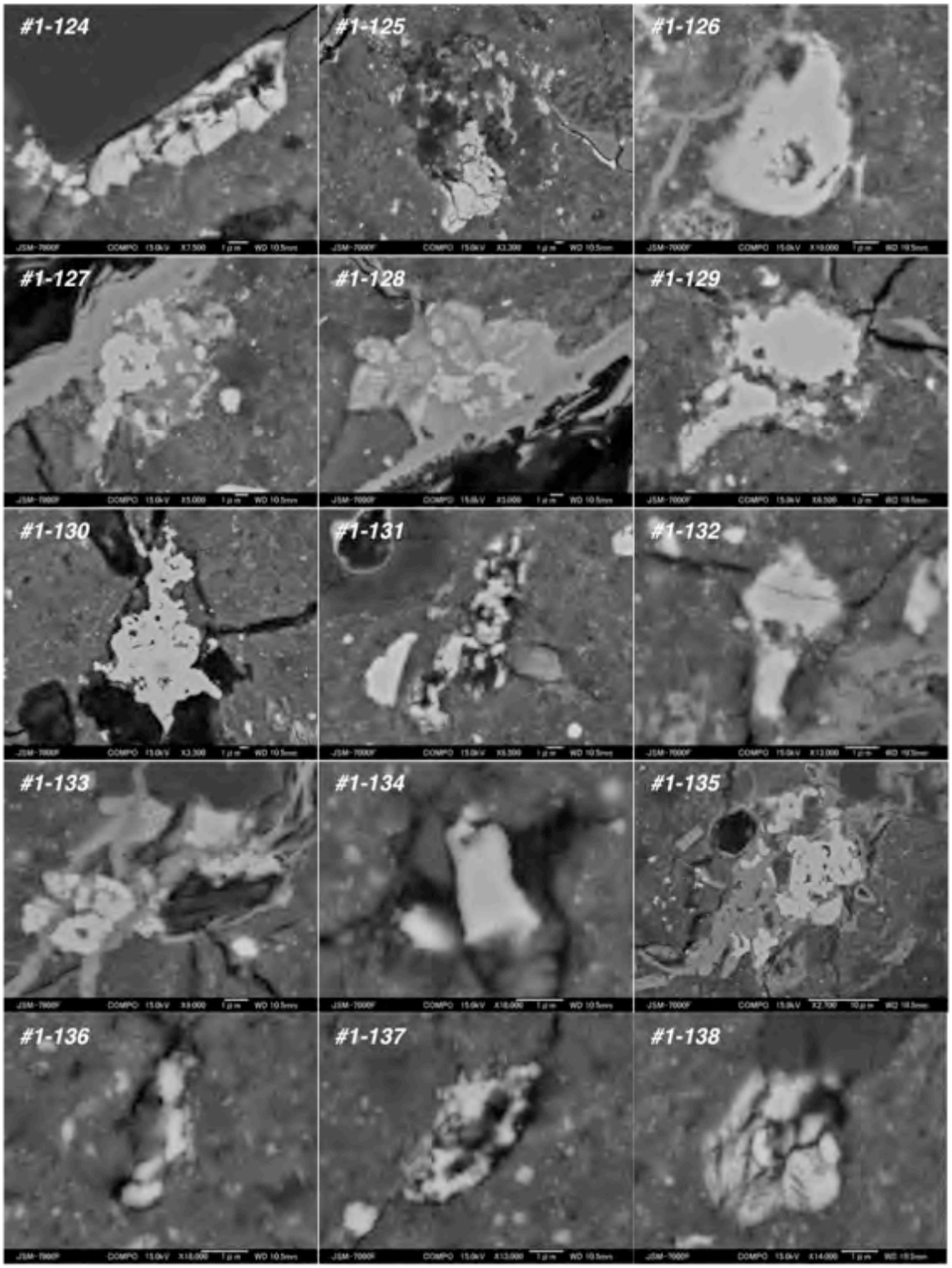

Fig. 28. (continued)

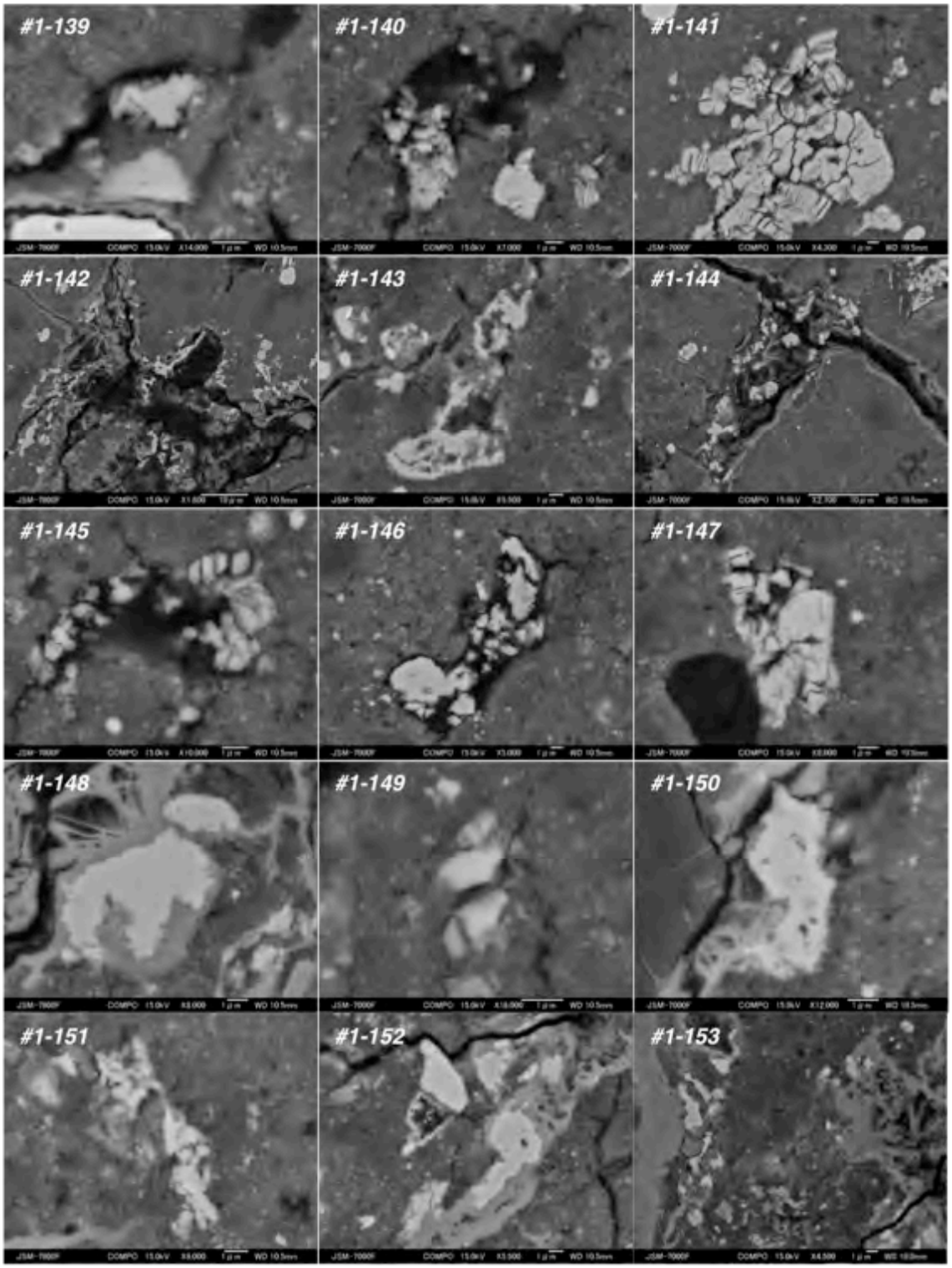

Fig. 28. (continued)

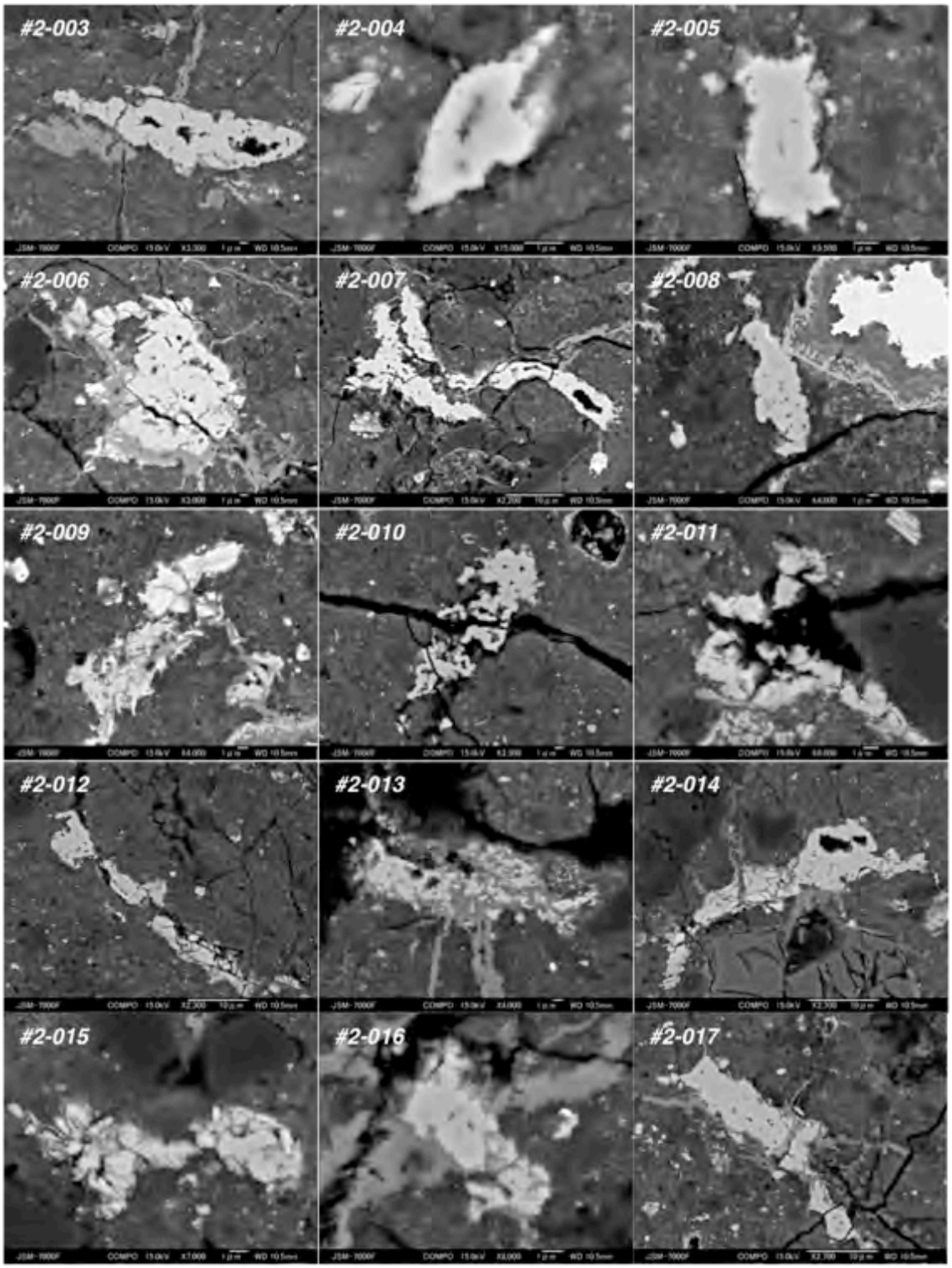

Fig. 28. (continued)

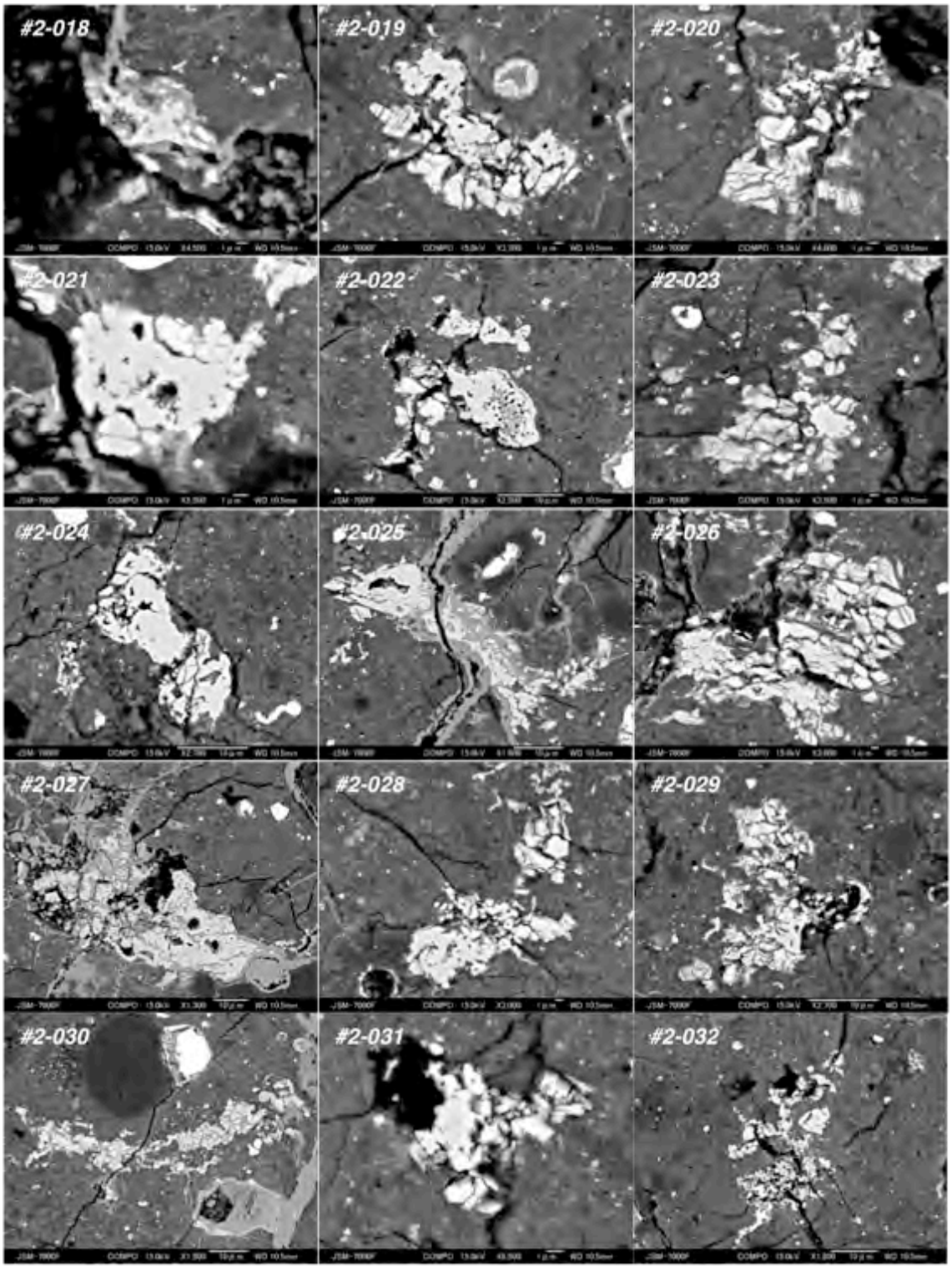

Fig. 28. (continued)

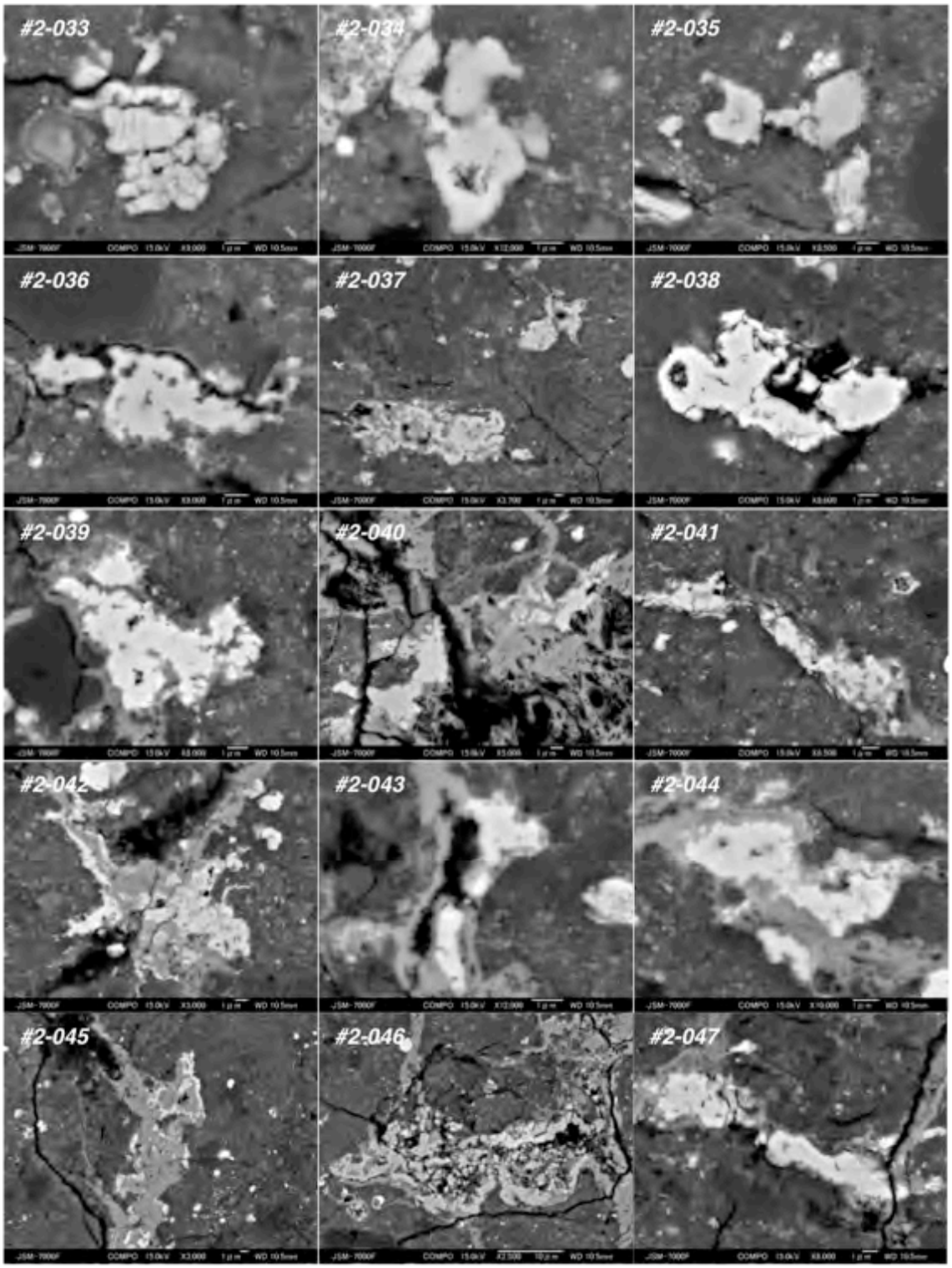

Fig. 28. (continued)

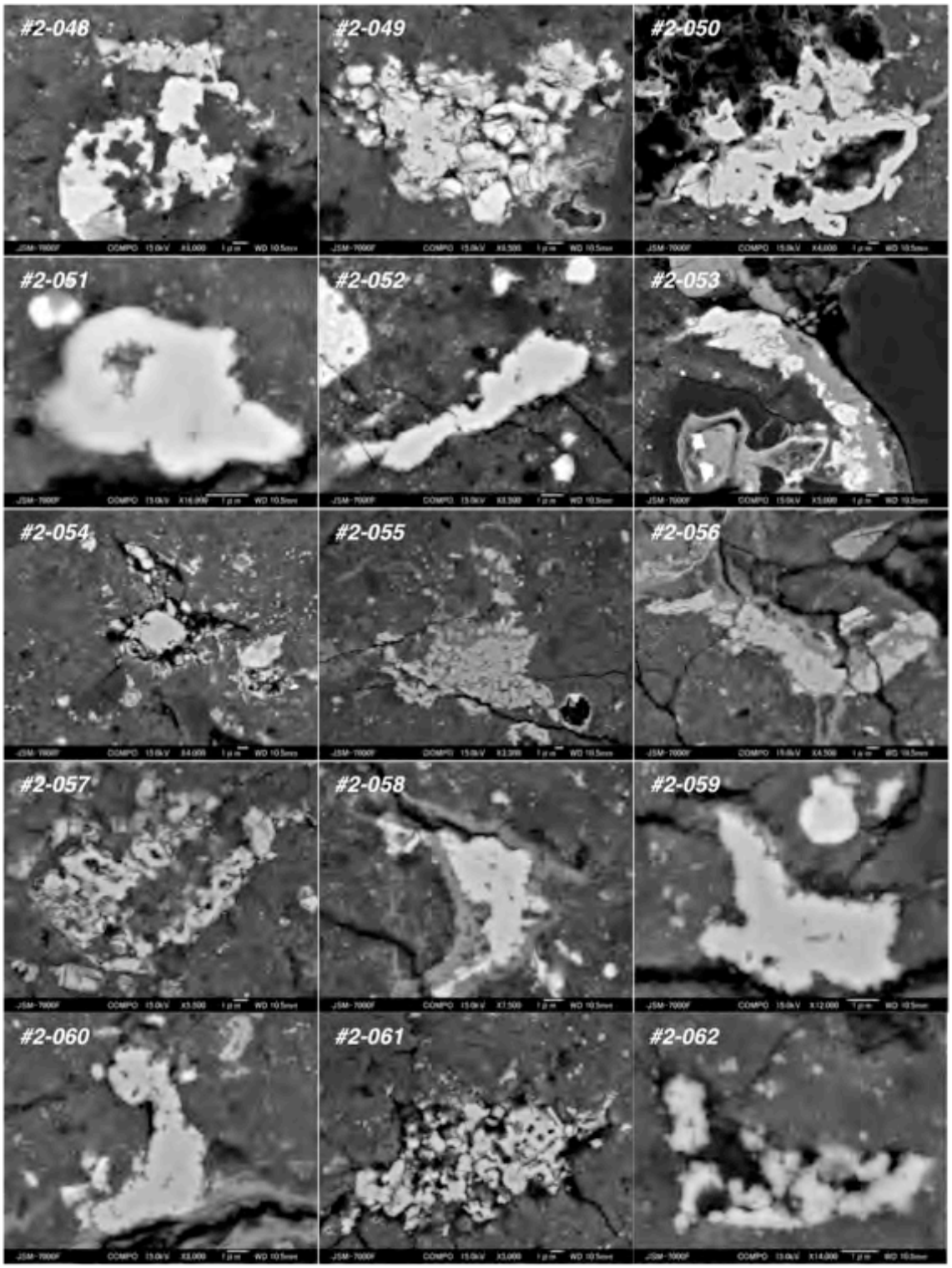

Fig. 28. (continued)

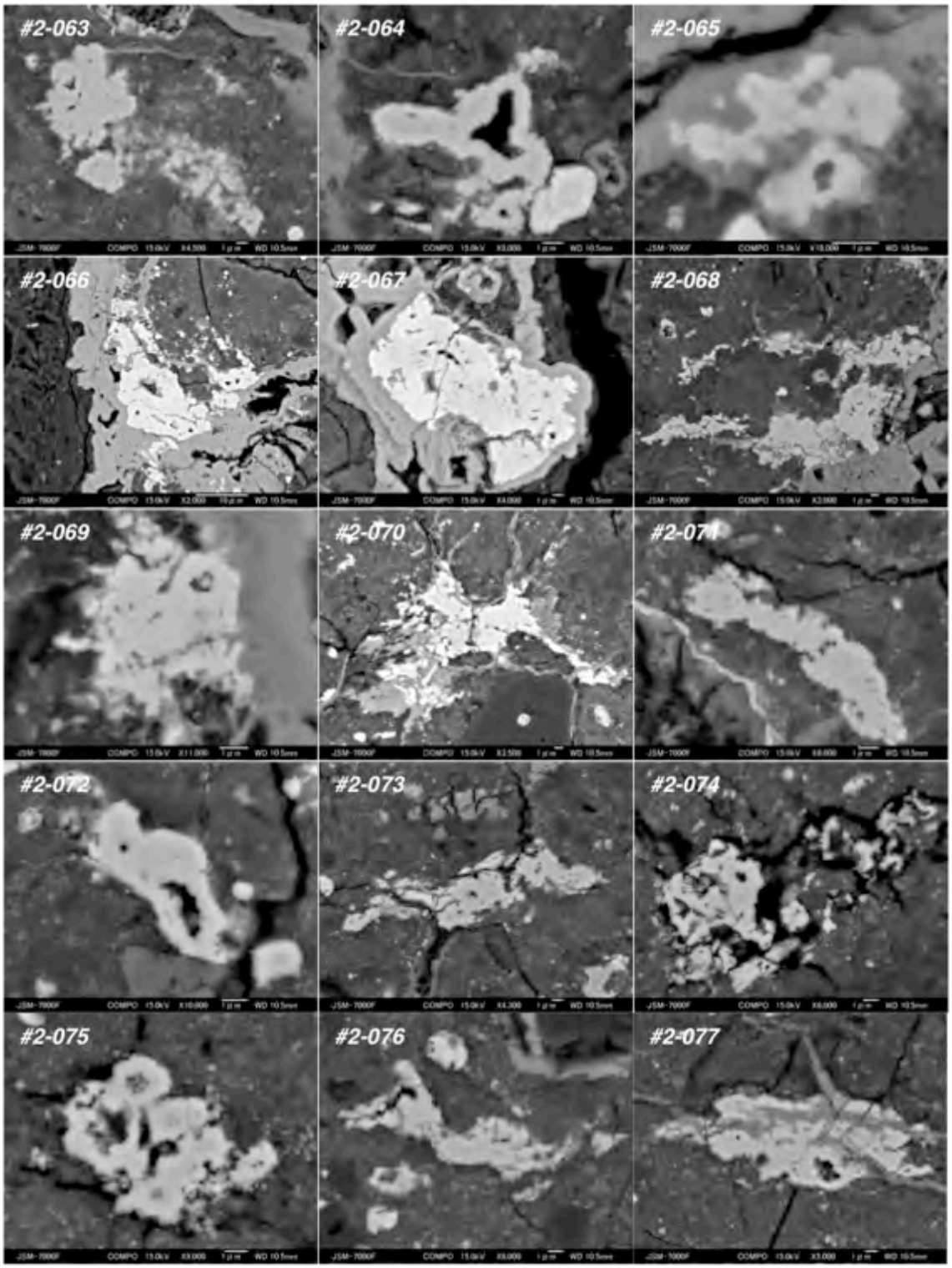

Fig. 28. (continued)

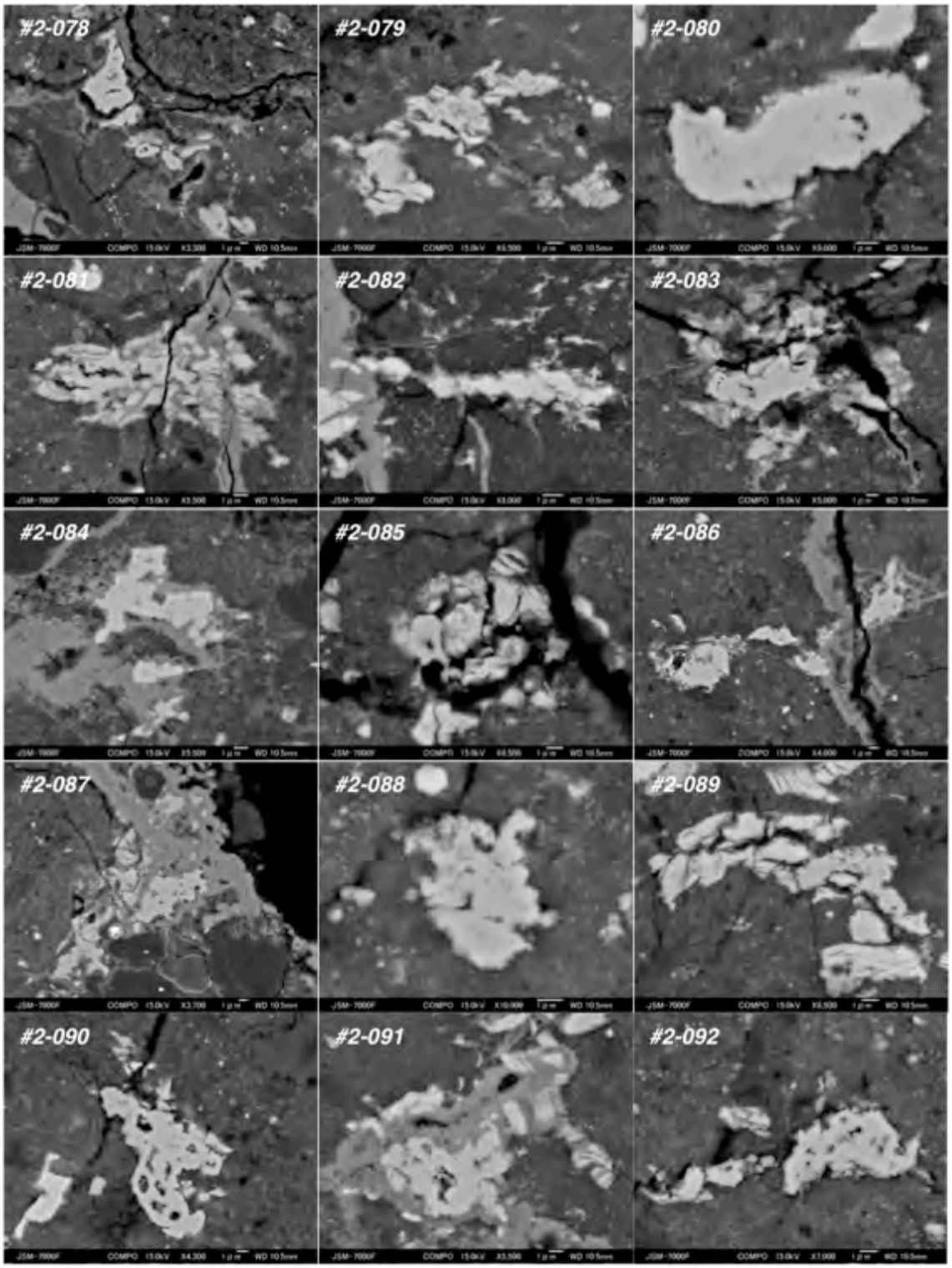

Fig. 28. (continued)

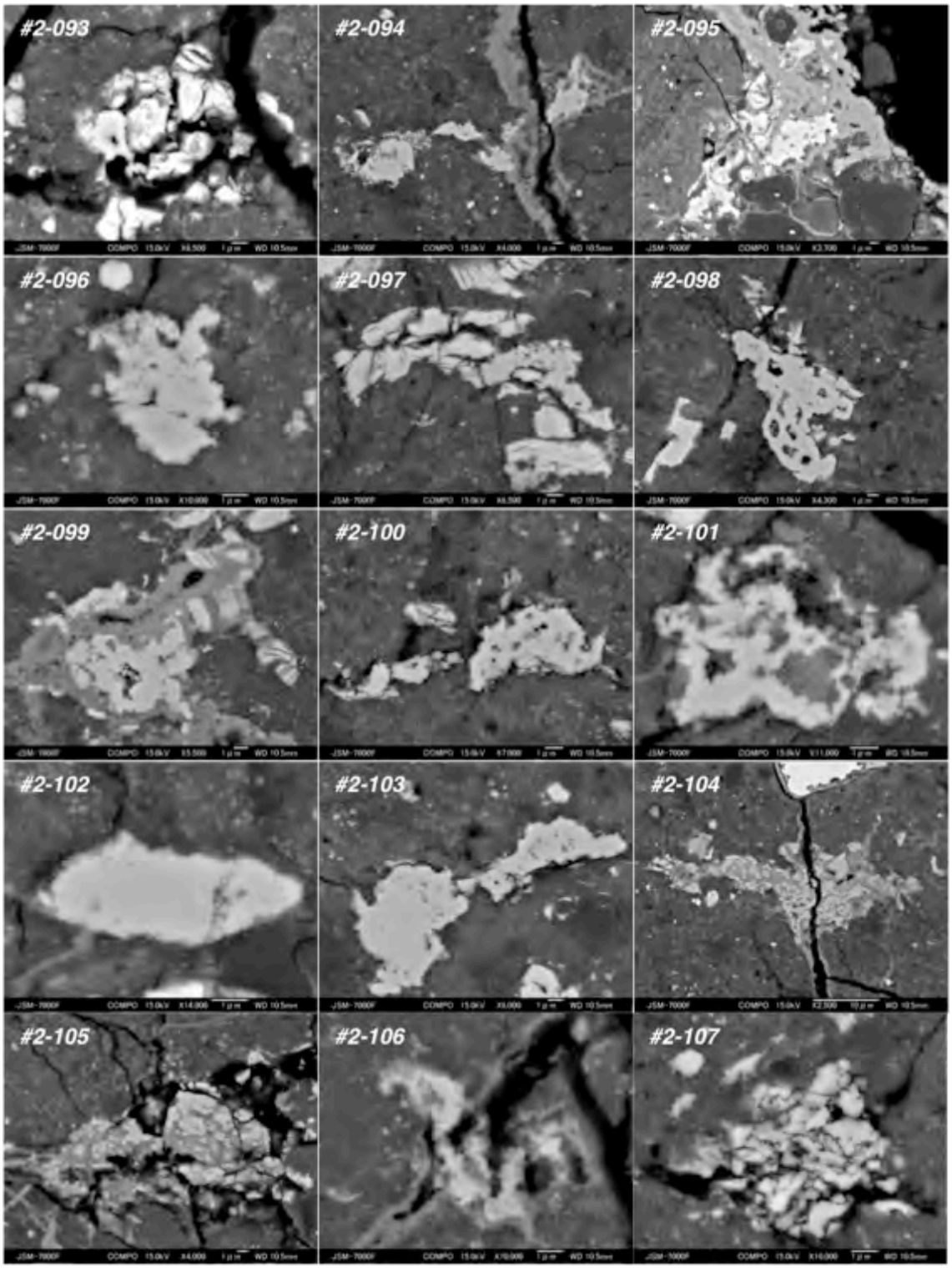

Fig. 28. (continued)

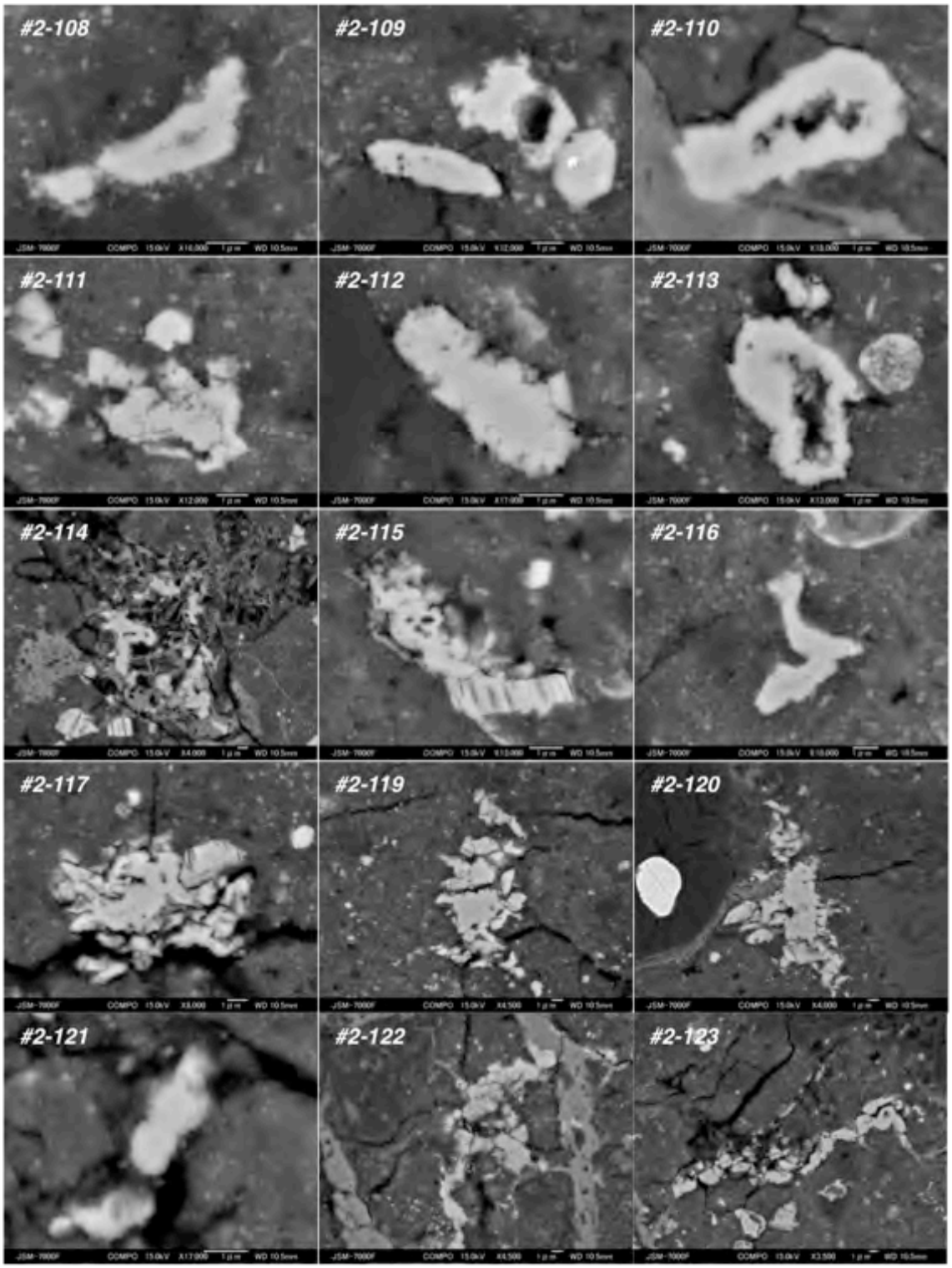

Fig. 28. (continued)

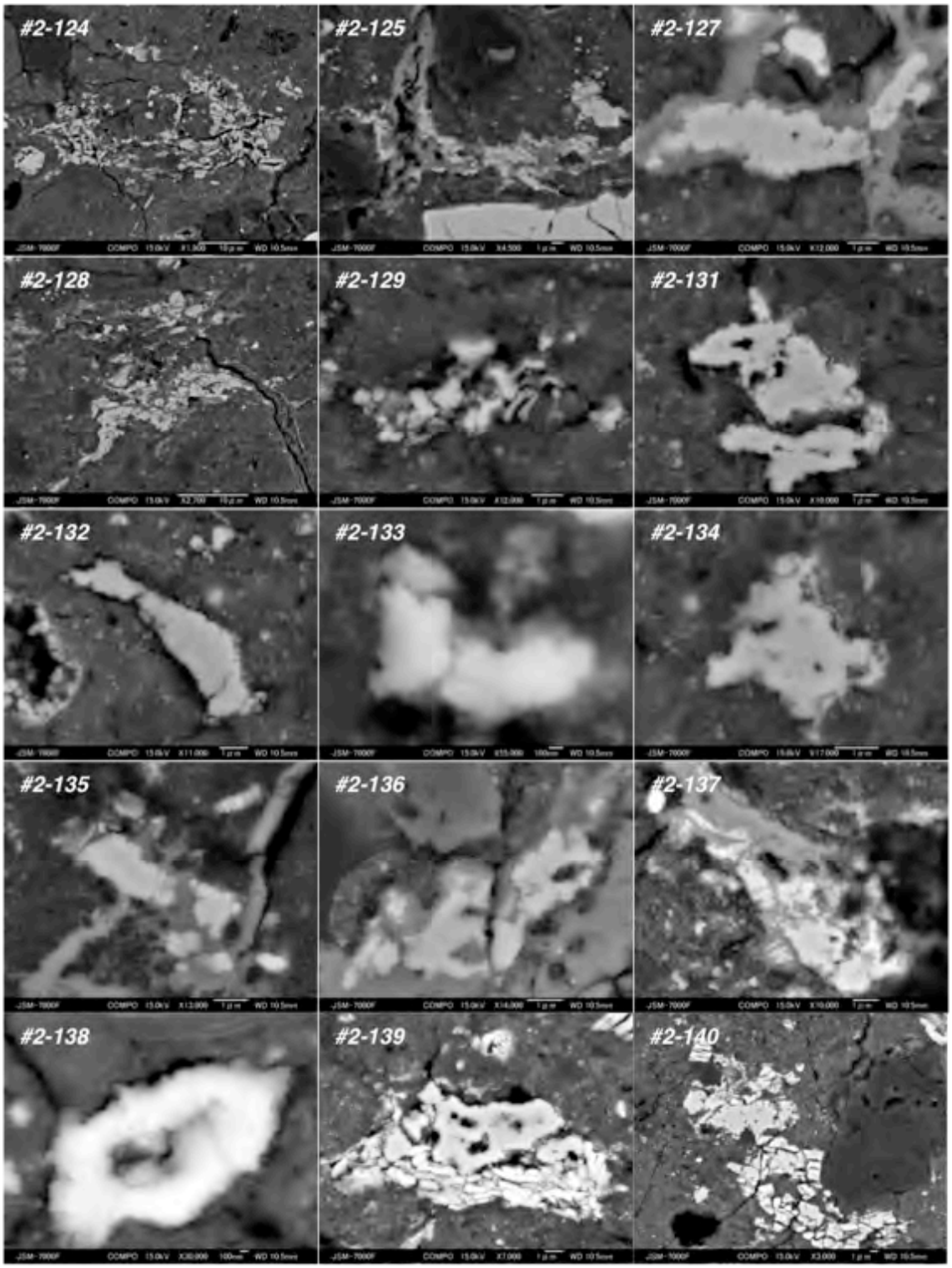

Fig. 28. (continued)

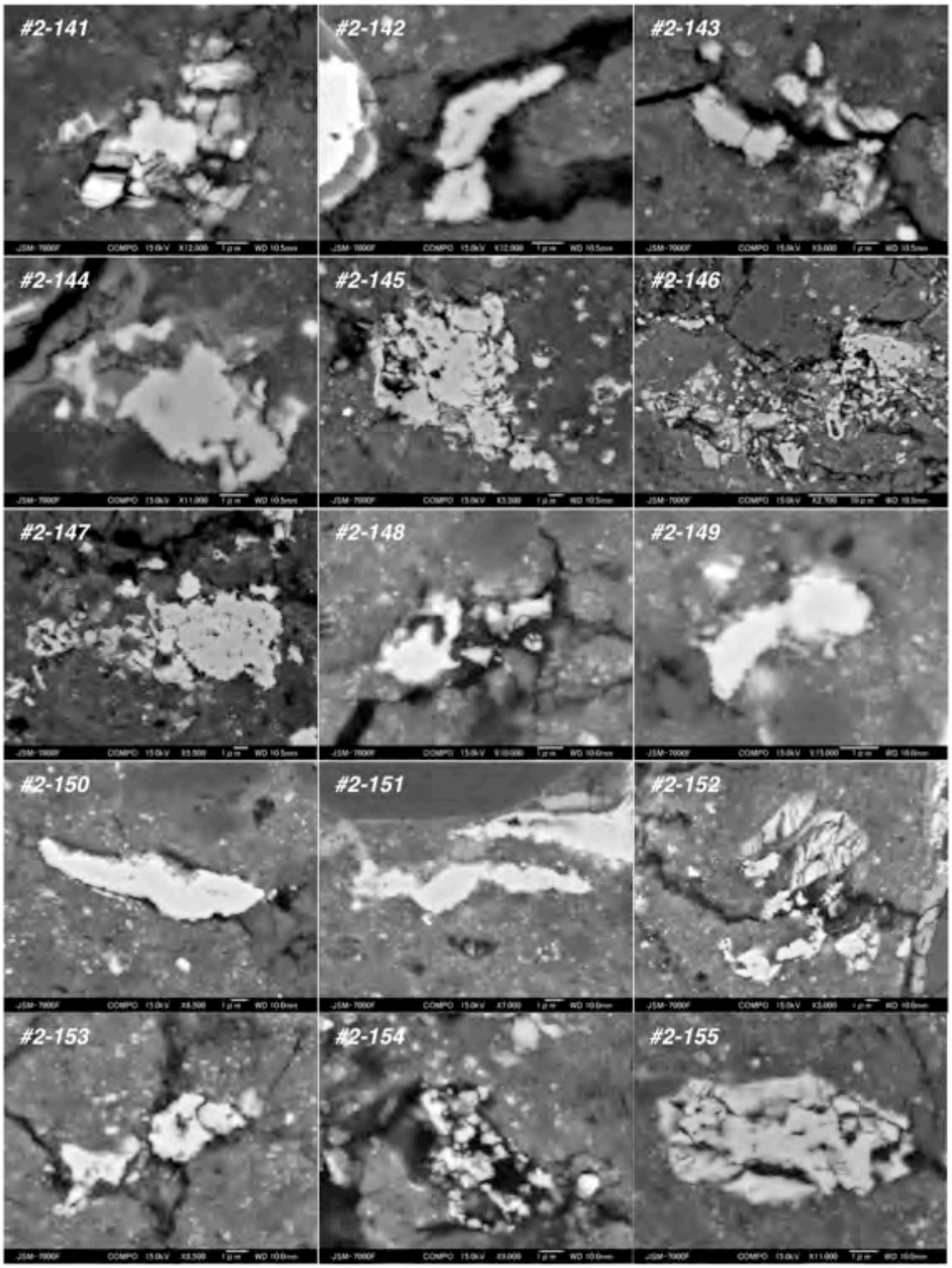

Fig. 28. (continued)

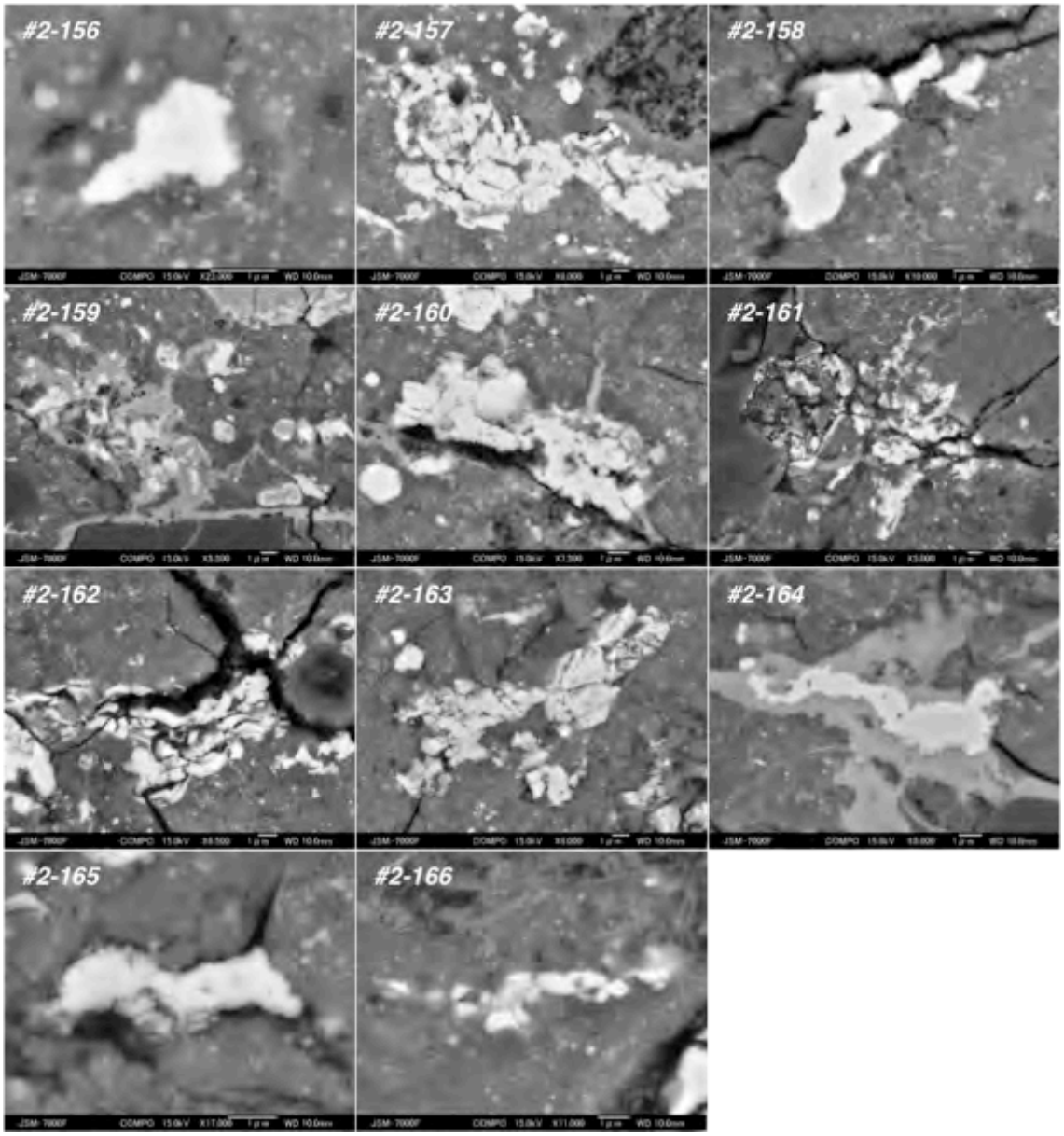

Fig. 28. (continued)

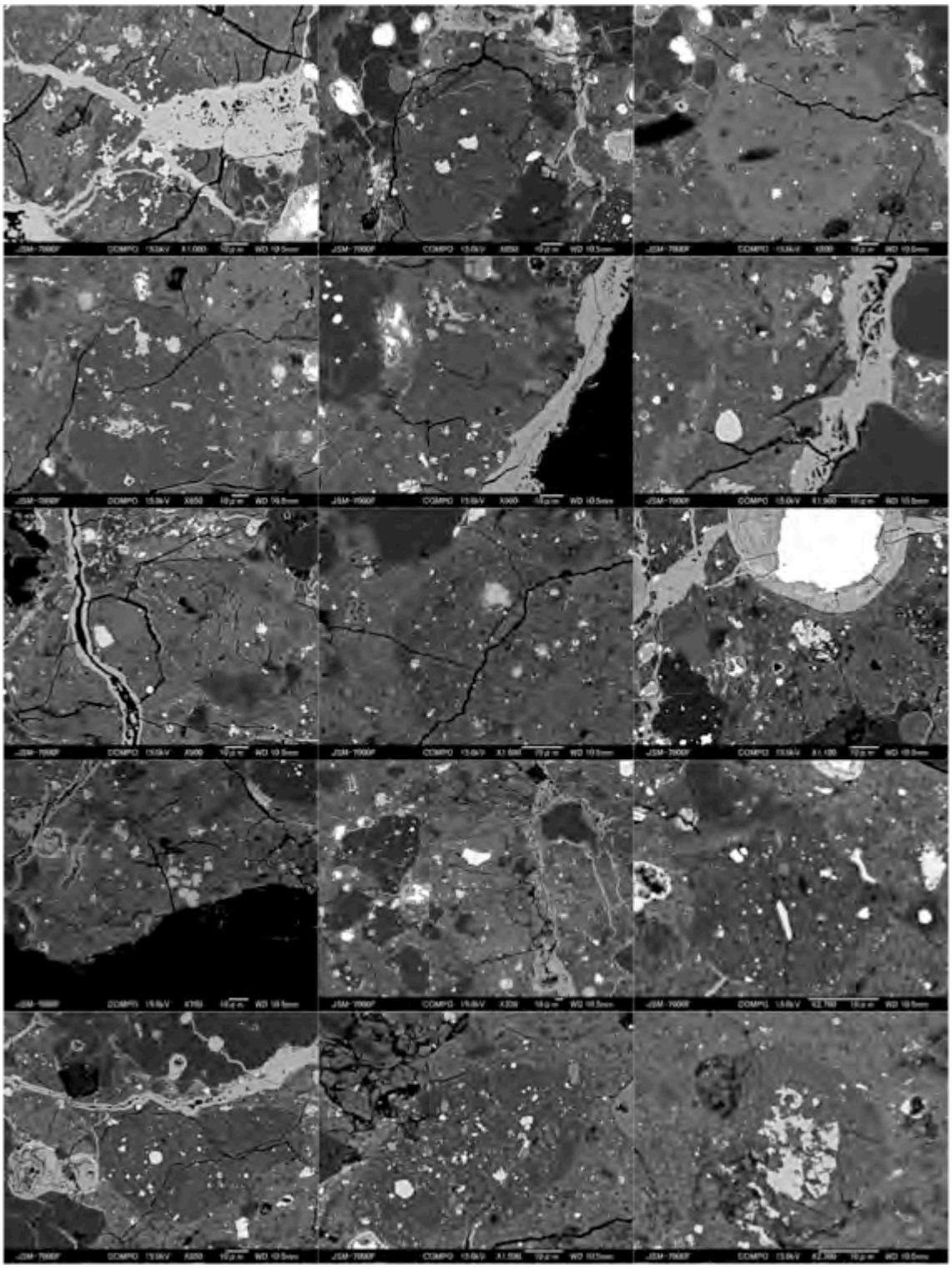

Fig. 29. Backscattered electron images of chondritic lithic clasts (dark inclusions) in the Acfer 094.